



**HAL**  
open science

## Field Application and Validation of a Seismic Bedload Transport Model

Maarten Bakker, Florent Gimbert, Thomas Geay, Clément Misset, Sébastien Zanker, Alain Recking

► **To cite this version:**

Maarten Bakker, Florent Gimbert, Thomas Geay, Clément Misset, Sébastien Zanker, et al.. Field Application and Validation of a Seismic Bedload Transport Model. *Journal of Geophysical Research: Earth Surface*, 2020, 125 (5), pp.e2019JF005416. 10.1029/2019jf005416 . hal-03107579

**HAL Id: hal-03107579**

**<https://hal.science/hal-03107579v1>**

Submitted on 12 Jan 2021

**HAL** is a multi-disciplinary open access archive for the deposit and dissemination of scientific research documents, whether they are published or not. The documents may come from teaching and research institutions in France or abroad, or from public or private research centers.

L'archive ouverte pluridisciplinaire **HAL**, est destinée au dépôt et à la diffusion de documents scientifiques de niveau recherche, publiés ou non, émanant des établissements d'enseignement et de recherche français ou étrangers, des laboratoires publics ou privés.



Distributed under a Creative Commons Attribution 4.0 International License

# Field Application and Validation of a Seismic Bedload Transport Model

**Key Points:**

- Bedload fluxes are derived independently from bank-side seismic measurements with an uncertainty factor of  $5^{\pm 1}$  for instantaneous values
- Simple experiments with large-rock impacts are used to calibrate seismic response and provide an alternative to instream bedload sampling
- Scaling seismic power with discharge allows bedload-generated vibrations to be isolated and gives insight into bedload temporal dynamics

**Supporting Information:**

- Supporting Information S1

**Correspondence to:**

M. Bakker,  
maartenbakker@yahoo.com






**Citation:**

Bakker, M., Gimbert, F., Geay, T., Misset, C., Zanker, S., & Recking, A. (2020). Field application and validation of a seismic bedload transport model. *Journal of Geophysical Research: Earth Surface*, 125, e2019JF005416. <https://doi.org/10.1029/2019JF005416>

Received 28 OCT 2019

Accepted 25 MAR 2020

Accepted article online 14 APR 2020

Maarten Bakker<sup>1,2</sup> , Florent Gimbert<sup>2</sup> , Thomas Geay<sup>3,4</sup> , Clément Misset<sup>1</sup> , Sébastien Zanker<sup>5</sup>, and Alain Recking<sup>1</sup> 

<sup>1</sup>University Grenoble Alpes, INRAE, ETNA, Grenoble, France, <sup>2</sup>University Grenoble Alpes, CNRS, IRD, Institute for Geosciences and Environmental Research (IGE), Grenoble, France, <sup>3</sup>BURGEAP, Grenoble, France, <sup>4</sup>University Grenoble Alpes, CNRS, INP, GIPSA-lab, Grenoble, France, <sup>5</sup>Électricité de France, DTG division, Grenoble, France

**Abstract** Bedload transport drives morphological changes in gravel-bed streams and sediment transfer in catchments. The large impact forces associated with bedload motion and its highly dynamic spatiotemporal nature make it difficult to monitor bedload transport in the field. In this study, we revise a physically-based model of bedload-induced seismic ground motion proposed by Tsai et al. (2012) and apply it to invert bedload flux from seismic measurements alongside an Alpine stream. First, we constrain the seismic response of a braided river reach with a simple active experiment using a series of large-rock impacts. This allows the characterization of surface wave propagation and attenuation with distance from the impact source. Second, we distinguish bedload-generated ground vibrations from those caused by turbulent flow using frequency-based scaling relationships between seismic power and discharge. Finally, absolute bedload transport rates are quantified from seismic measurements using inverse modeling based on a simplified formulation of bedload particle motion. The results are verified with a large data set of bedload samples, demonstrating that seismic measurements can provide an indirect measure for bedload flux with uncertainties within a factor of  $5^{\pm 1}$  for instantaneous measurements (between 0.01 and 1 kg/m/s). Larger deviations may be caused by uncertainties in the contribution of turbulent flow effects, particle impact velocity, and especially particle size that may vary with sediment supply and flow conditions. When constraining these uncertainties, instream sediment transport measurements are no longer necessarily required and seismic monitoring may provide an accurate and continuous means to investigate bedload dynamics in gravel-bed streams.

## 1. Introduction

Sediment transport in gravel-bed rivers is characterized by highly dynamic bedload processes that lead to largely fluctuating transport rates (Gomez et al., 1989; Hoey, 1992). Quantifying bedload transport rates in both space and time is critical for the understanding of sediment transfer and coupled morphodynamics in river systems (Ashmore, 1991; Ashmore & Church, 1998; Williams et al., 2015), particularly in Alpine environments with high energy and sediment availability (e.g., Lane et al., 1996). The storage and/or release of riverbed material may affect riparian habitats and land usage through riverbed aggradation/degradation (Bakker et al., 2018) and lateral channel dynamics (Church, 2006). More directly, bedload impacts pose a direct hazard not only to infrastructure, including bridges and bank protection (Badoux et al., 2014), but also to instream measurement equipment that may be subject to damage or failure, particularly during high-magnitude events. As such, there are only a limited number of sites with continuous bedload measurements (e.g., Mizuyama et al., 2010; Rickenmann et al., 2014). In order to acquire the necessary field data and to overcome practical limitations of direct measurements, seismic techniques have been proposed to provide an indirect measure of bedload transport.

The first evidence that bedload transport may be detected in seismic data was provided by Govi et al. (1993). Some 15–20 years later, more extensive seismic measurements were made and explored for the frequency response of processes that generate seismic ground vibrations, most notably bedload transport and flow turbulence (Burtin et al., 2008; Burtin et al., 2011; Schmandt et al., 2013). The fundamental basis for the quantitative applications is provided by Tsai et al. (2012), who developed a physically-based model and invert bedload transport from the seismic response it generates, and Gimbert et al. (2014), who complemented this work with the modeling of turbulent flow that drives bedload transport.

© 2020. The Authors.

This is an open access article under the terms of the Creative Commons Attribution License, which permits use, distribution and reproduction in any medium, provided the original work is properly cited.

The bedload model by Tsai et al. (2012) has been verified to be applicable for the quantification of low bedload transport rates in controlled flume-based experiments (Gimbert et al., 2019). However, the model has yet to be independently tested in the field. For those studies where field observations are available, notably streams equipped with continuously monitoring Swiss plate geophone systems, empirical regression techniques (Roth et al., 2016; Roth et al., 2017) and Monte Carlo-based modeling approaches (Dietze et al., 2019) were employed to quantify seismic response. However, the quantitative link with physical constraints was not investigated. Where no direct field observations were available or possible, a physically-based approach was used to study transport during high-flow events associated with typhoons (Chao et al., 2015), a monsoon season (Burtin et al., 2008; Tsai et al., 2012), and a glacial outburst flood (Cook et al., 2018). In this study, we aim to reconcile and combine these approaches by assessing bedload transport rates inverted from seismic measurements with independently sampled bedload fluxes.

The goal of this paper is to evaluate how well bedload transport in a typical Alpine gravel-bed stream can be constrained and quantified with seismic techniques. We assess the application of the theoretical seismic bedload transport model of Tsai et al. (2012) in a field setting, a braided reach of the Séveraisse River in the French Alps. A two-step approach is followed to validate the model. First, we characterize the seismic response of the riverbed through a simple active experiment using a series of large-rock impacts. Second, we use this to quantify bedload flux from seismic records using a physically-based bedload saltation model. We compare the inverted fluxes to an extensive set of bedload samples at this site (Misset et al., 2020), demonstrating that a relatively simple seismic approach can provide a viable field technique to continuously monitor bedload transport processes.

## 2. Study Area and Data Availability

The Séveraisse River is a natural Alpine stream that flows from the Ecrins Massif in the French Alps. It has a catchment area of  $\sim 130 \text{ km}^2$  with the largest flows generated during spring snow melt and summer thunderstorms. We studied a braided river reach approximately 600 m long and up to 90 m wide (Figure 1) that lies at an elevation of just above 1,000 m a.s.l., near the village of Villar-Loubière. The riverbed has a gentle gradient of  $\sim 1\%$  and is largely composed of gravel at the surface and includes finer material in the subsurface (Misset et al., 2019). The particle-size distribution of the riverbed in the braided reach was determined by Misset et al. (2020) and is shown in Figure 2.

At the bridge just downstream of the braided reach (Figure 1), the electricity company Électricité de France (EDF) operates a gauging station that provides stage and discharge measurements at 10-min resolution. The

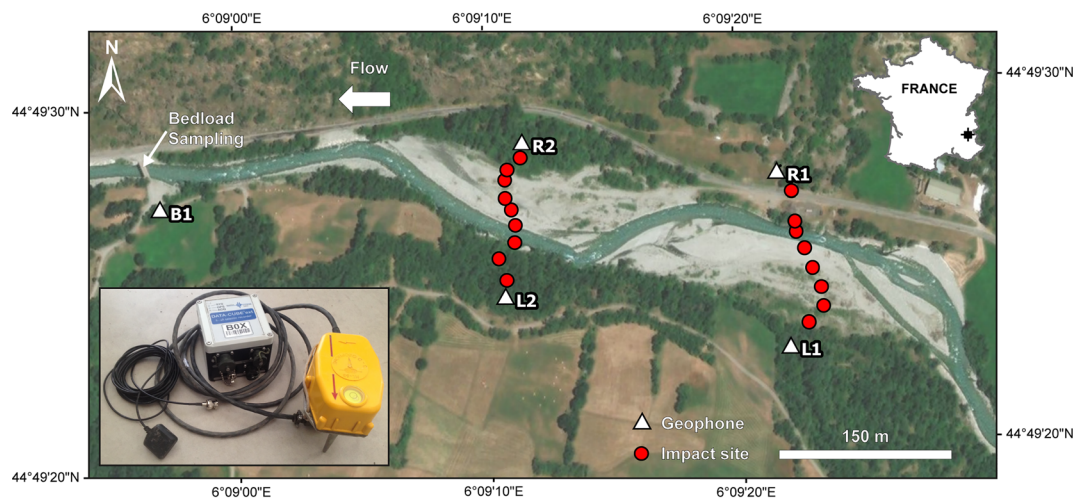


**Figure 1.** Aerial image (courtesy of Esri-World Imagery) of the studied reach of the Séveraisse River, France, with latitude and longitude coordinates on the x and y axes. Geophones locations L1, L2, R1, and R2 are shown, which were used for seismic characterization based on large-rock impacts along cross sections between the geophones on opposite banks. At the downstream end of the reach, bedload sampling was performed and bedload transport is quantified from measurements at geophone B1. Inset image of geophone (right), logger (center), and GPS (left bottom).

channel here is straight and laterally confined, 12 m wide, and the riverbed is covered with cobbles that have an intermediate diameter  $D_{50} = 11$  cm and  $D_{84} = 30$  cm as derived from Wolman counts (particles sampled at a fixed interval, e.g., every 1 m, along a transect) by Misset et al. (2020). Misset et al. (2020) also performed an extensive bedload sampling campaign from the bridge (Figure 2; inset). Data are available from 60 cross-sectional averaged bedload samples that were taken during a range of flow conditions ( $9\text{--}25$  m<sup>3</sup>/s) in the period 23 April to 26 June 2018. For 16 of these samples (240 kg in total), they also provide a particle-size distribution by weight (Figure 2). In this study, we consider the measured bedload transport flux for the particle size range 1.6–91 mm. Both finer and coarser particles might not be efficiently captured during sampling due to the size of the mesh (0.5 mm) and mouth of the sampler ( $20.7 \times 12$  cm). Whereas the sand fraction has a negligible contribution to the seismic signal (Tsai et al., 2012), the load of the coarse fraction ( $>91$  mm) may be estimated through extrapolation using the particle-size distribution from mobile braided river bars (Parker & Klingeman, 1982) and accounts for 22% of the total load based on the data of Misset et al. (2020). Following Kellerhals and Bray (1971), particle-size distributions found using volume by weight (sampled bedload of 91 mm and smaller) and grid by number (Wolman counts of riverbed) approaches are comparable, which is indeed confirmed in Figure 2.

### 3. Methods

#### 3.1. Seismic Field Setup and Processing

In the period May–October 2018, five 3-component Sensor PE-6/B geophones registered ground motion at a distance of 25–50 m from the channel edge (Figure 1). Four geophones were placed along the braided reach and one besides the bridge where bedload sampling was performed. They were installed ~30 cm in the ground, oriented north and leveled horizontally. We study Rayleigh surface waves using measurements of the vertical component. The geophones allow seismic measurements over a frequency range from 4.5 Hz to  $>100$  Hz, which is expected to be suitable for the observation of bedload transport at the considered distance (Burtin et al., 2011; Gimbert et al., 2014). Data from the geophones were recorded with a frequency of 400 Hz on a DiGOS DATA-CUBE logger, allowing the assessment of vibrations up to 200 Hz. The logger

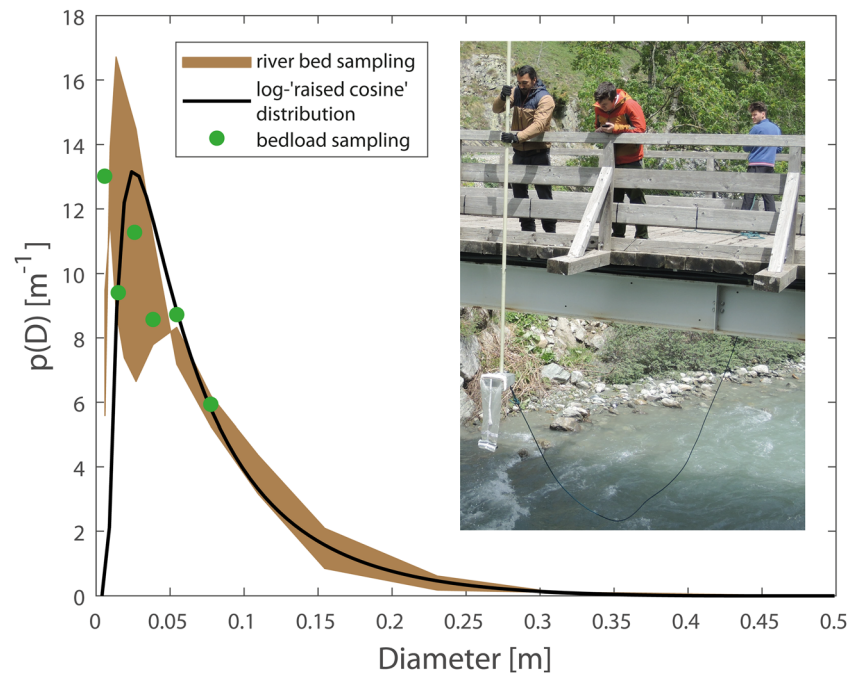


**Figure 2.** Particle-size distribution of mobile braided river bars, where the range is based on the May and June 2018 Wolman counts (400 particles) of surface particle size, and the sampled particle-size distribution of bedload material in transport (truncated at 91 cm), both performed by Misset et al. (2020). A log-“raised cosine” distribution (Tsai et al., 2012) with  $\mu = 0.055$  m and  $\sigma = 0.75$  was visually fitted to the data. The photo inset shows bedload sampling from the bridge using an Elwah sampler.

was configured with an amplifier gain of 16. Simultaneously, an active GPS antenna (BY-GPS-07) was used to register time, allowing the precise synchronization of the measured records from the geophones at the different sites.

The raw seismic signal (counts) exported from the logger is converted to vertical ground velocity  $V$  (m/s) due to seismic ground vibrations by considering the logger and the geophone sensitivities according to manufacturer specifications. To analyze the seismic signal in both time ( $t$ ) and frequency ( $f$ ) domains, the power spectral density  $P$  is determined as equation 1:

$$P(f) = \frac{|V(f)|^2}{T}, \quad (1)$$

where  $V(f)$  is the Fourier transform of  $V(t)$  over a time window with duration  $T$ . We use the method of Welch (1967) to compute  $P$ , which is based on a fast Fourier transform and averages power using three overlapping time subwindows with 50% overlap to reduce the variance in the computed spectrogram following Burtin et al. (2016). The temporal resolution  $T$  over which power is determined is 1 s for the active drop-experiment and 3 s for bedload monitoring. For the long-term bedload monitoring, we aggregate the signal to a 10-min resolution by taking the median  $P$  value, which allows the effects of episodic and short-lived, strong-energy signals, for example, the passing by of people, animals, or vehicles, to be excluded from the time series.

### 3.2. Seismic Framework

Following Tsai et al. (2012), we use a general seismic framework to relate the impact force of particles on the riverbed to seismic power measured on the riverbank through seismic wave generation and propagation. The absolute vertical ground velocity  $V$  of seismic ground vibrations with wave frequency  $f$  may be described as equation 2:

$$|V(f, r)| = 2\pi f F(f) G(f, r) Z(f), \quad (2)$$

where  $F$  is the vertical component of the impact force exerted on the riverbed,  $G$  is the Green's function that converts force to ground velocity and describes the frequency-dependent wave attenuation with radial distance  $r$  from the source, and we introduce  $Z$  as a site-specific amplification factor that was not specified in Tsai et al. (2012) and which we will discuss later.

The impact force of a typical bedload particle may be considered as instantaneous because relative impact duration (milliseconds; Johnson, 1987) is expected to be much shorter than the considered seismic wave period (tens of milliseconds). In that case, force is a dirac, that is, it is no longer a function of frequency and can be described as equation 3 (Tsai et al., 2012):

$$F = mu\gamma, \quad (3)$$

where  $m$  is the mass of the particle,  $u$  is its vertical impact velocity, and  $\gamma$  is a factor that accounts for the elasticity of the particle impact where  $\gamma = 1$  corresponds to a perfectly inelastic impact and  $\gamma = 2$  to a perfectly elastic impact.

The Green's function for Rayleigh waves is expressed as equation 4 (Aki & Richards, 2002; Tsai & Atiganyanun, 2014):

$$G(f, r) \approx \frac{Nk}{8\rho_s v_p v_g} \sqrt{\frac{2}{\pi kr}} e^{-\frac{\pi fr}{v_g k}}. \quad (4)$$

This function describes wave amplitude decrease due to two-dimensional spreading  $\sqrt{2/\pi kr}$  in the far-field domain (wavelength  $\lambda = v_p/f \gg r$ ), where  $k$  is the angular wavenumber (rad/m), equation 5a, and inelastic attenuation of waves as they propagate into the ground.  $N$  is a function of the surface wave eigenfunction which was approximated to unity by Tsai et al. (2012) and which was later supported by numerical modeling in Tsai and Atiganyanun (2014) for frequencies of 10–50 Hz that are typically associated with bedload. The

density of sediment  $\rho_s$  is 2,650 kg/m<sup>3</sup>,  $v_p$  is the wave phase velocity, equation 5b,  $v_g$  the wave group velocity, equation 5c, and  $K$  is the dimensionless quality factor, which is an intrinsic material parameter that accounts for inelastic energy loss, equation 5d.

$$k = 2\pi f / v_p, \quad (5a)$$

$$v_p = v_{p0} (f/f_0)^{-\xi}, \quad (5b)$$

$$v_g = v_p / (1 + \xi), \quad (5c)$$

$$K = K_0 (f/f_0)^\eta. \quad (5d)$$

Tsai et al. (2012) used normalized wave velocity functions ( $f_0 = 1$  Hz) and provided standard values of  $v_{p0} = 1295$  m/s ( $v_p$  at 1 Hz) and  $\xi = 0.374$ , a dimensionless exponent that is used to quantify the frequency-dependency decay, based on depth-velocity profiles for a generic bedrock subsurface (Boore & Joyner, 1997). It is uncertain however to which extent such approximation applies to river settings that contain sedimentary layer(s) in the subsurface. Lastly, Tsai et al. (2012) assumed a constant  $K = 20$  for the relatively high frequencies of interest, that is,  $K_0 = 20$  ( $K$  at 1 Hz) and a dimensionless exponent  $\eta = 0$ , equation 5d, based on Anderson and Hough (1984). Note that the term  $K$  is referred to as  $Q$  in Tsai et al. (2012), but that here  $Q$  is used for discharge. For the local application of the seismic framework, the functions and the values of the constituent parameter values given here have substantial uncertainties associated with them and we therefore seek to quantify them for our field site by means of an active seismic experiment.

### 3.3. Active Seismic Experiment

An active experiment is used to characterize riverbed seismic wave propagation and attenuation such that we can constrain ground velocity ( $V$ ) due to an impact force ( $F$ ) following Tsai et al. (2012). Although there are various advanced seismic sources and configurations (e.g., Park et al., 2007; Rix et al., 2002) that may be used to perform active seismic experiments, we chose a basic and practical approach. The experiment was performed during low-flow conditions (mean discharge 4.5 m<sup>3</sup>/s) and consisted of the repetitive dropping of a large rock on the dry riverbed, 10 drops at each site, at well-defined distances along a cross section between geophones located on opposite banks (Figure 1). The rock had a mass of 17.4 kg and was dropped from a height of approximately 1.6 m (operator shoulder height). Based on our experiences, we assume purely inelastic impacts ( $\gamma = 1$ ) as the rock generally rebounds very slightly of the surface and there is only minor loss in vertical energy transfer due to the rock glancing off or rotating after impacting upon the undulating surface. With this drop-experiment, we specifically seek to quantify  $v_g$ ,  $v_p$ , and  $K$  in the Green's function, equation 4, and the amplification factor  $Z$  for the braided reach, equation 2, as a function of frequency.

First, a wave group velocity dispersion curve is determined based on identifying rock-impact arrivals at geophones on opposite banks for various frequency intervals (e.g., Ritzwoller & Levshin, 1998). The raw seismic time series (in counts) are band-pass filtered for 50% overlapping intervals of 6 Hz, using a first-order filter, and the signals are bounded using a Hilbert transform envelope for which we picked the peak values. With this technique, the selected mode is a priori unknown and corresponds to the mode with the highest energy. Nevertheless, we assume that the fundamental mode dominates the energy over the investigated frequency range, which we verify a posteriori with the form of the inferred dispersion curve (absence of discontinuities). To ensure a significant time delay between arrivals on opposite banks (and reduce uncertainty due to the limited temporal resolution of the measurements), we use the impacts closest to one or other sensor on each bank (Figure 1) for which the registered peak is above the ambient noise level on both banks (we confirm our results with the second nearest impact sites). We relate the delays to known source-to-receiver distances (geophone and impact locations were measured with a differential GPS; Figure 1) in order to calculate wave group velocity.

Second, the quality factor  $K$  is determined through fitting the decay of seismic power with distance. We correct for background noise (period before and after drop events) and we normalize  $P$  to avoid any effects

related to signal amplitude and distance (see Supporting Information S2). The value of  $K$  is derived and we assess its frequency dependency (e.g., Erickson et al., 2004), that is, the value of  $\eta$  (equation 5d).

Third, we quantify  $Z$  to account for potential site amplification effects that may occur due to the trapping of seismic waves in sedimentary layers or in the structure of the basin topography (e.g., Roten et al., 2004). We effectively use  $Z$  as a semi-empirical factor to calibrate the seismic amplitude of the impacts in a field setting, and therefore, it also includes the errors associated with the assumed values of factors  $N$  and  $\gamma$ .  $Z$  is quantified with equation 2 using the locally derived Green's function (equation 4) and the prescribed impact force that the rock exerts on the bed surface (equation 3). The force is derived from the known mass of the rock and an estimate for the impact velocity  $u = \sqrt{2gh_i}$  when it is released from height  $h_i$  ( $g$  is the acceleration due to gravity). To facilitate this simple experimental design, we (1) performed the impacts on the dry riverbed, not in the water, and (2) we use a large rock, relative to the surface material and relative to surface deformations upon (repetitive) impact, to minimize impact force energy losses upon impact with the unconsolidated sedimentary surface (Bachelet et al., 2018; Kean et al., 2015). Finally, an additional small-scale drop experiment, consisting of five drops at five distances (30–70 m), was performed at site B1 to verify local site amplification effects.

### 3.4. Physically-Based Bedload Transport Model

To couple seismic measurements to bedload flux, we require a particle-based approach. The model used by Tsai et al. (2012) was taken from physically-based and flume-based studies that investigated bedload saltation for the application in studies on fluvial bedrock incision (Lamb et al., 2008; Sklar & Dietrich, 2004). Saltation is considered the dominant mode of bedload transport, even at low transport rates (Lajeunesse et al., 2010), and is thus expected to be suitable to quantify bedload flux. Using a particle-based approach, the (downstream) bedload flux can be coupled to the particle impacts perpendicular to the bed surface as equation 6a:

$$q_b(D) = \frac{mJL}{W}, \quad (6a)$$

$$q_b(D) = \frac{mJU_b h_b}{c_a u_s W}, \quad (6b)$$

where  $q_b$  (kg/m/s) is the fractional (particle size dependent) bedload transport per meter width  $W$ , for spherical particles with mass  $m = \rho_s(\pi/6)D^3$  and where  $D$  is the particle diameter. Further,  $J$  is the particle impact rate per unit channel length ( $\text{m}^{-1}\text{s}^{-1}$ ) and  $L$  is the saltation hop length. Here, we revisit the transport model, staying with the essence of this formula 6a and estimating  $L$  based on recent particle tracking experiments. Tsai et al. (2012) used an expanded version of this formula with separate (semi)empirical descriptions of bedload layer velocity ( $U_b$ ), height ( $h_b$ ), particle ascent time ( $c_a$ ), and settling velocity ( $u_s$ ) based on Sklar and Dietrich (2004), equation 6b (we do not use this formula except where we explore the general sensitivity and uncertainty of bedload inversions). Note we also determine  $q_b$  in kg/m/s, whereas Tsai et al. (2012) consider volumetric bedload transport rates. Before we can quantify  $q_b$  for a given particle size, we will first present a flume-based expression for  $L$  and  $u$ , the latter which is used in the subsequent derivation of  $J$  from seismic power  $P$  measured in the field.

As a basis to quantify physical bedload saltation parameters (e.g., hop length), we use scaling functions based on transport stage (Abbott & Francis, 1977), which is the ratio between the dimensionless shear stress  $\tau^*$  at the bed surface, equation 7a, and the critical value  $\tau_c^*$  that is required to entrain particles with diameter  $D$ .

$$\tau^*(D) = \frac{hS}{sD}, \quad (7a)$$

$$\tau_c^*(D) = \tau_{cD_{50}}^* \left( \frac{D}{D_{50}} \right)^{-0.9}, \quad (7b)$$

where  $h$  is flow depth at which bedload transport occurs,  $S$  is the riverbed slope, and  $s$  is the submerged specific density of the bedload material,  $s = (\rho_s - \rho_w)/\rho_w$ , where  $\rho_w$  is  $1,000 \text{ kg/m}^3$ . For the critical dimensionless shear stress, we use  $\tau_{cD_{50}}^* = 0.047$ , derived using the slope-dependent function proposed by Lamb et al. (2008), and take into account particle size effects at the riverbed surface with respect to the median size ( $D_{50}$ ), according to Parker (1990), equation 7b. Through equating equations 7a and 7b, we solve for water depth and discharge that is required for the onset of particle motion. In this study, we propose to quantify both hop length  $L$  and impact velocity  $u$  as a function of transport stage.

The hop length of a saltating bedload particle can be defined as equation 8:

$$L(D) = a_L D \left( \frac{\tau^*}{\tau_c^*} - 1 \right)^{b_L} \text{ for } \tau^* > \tau_c^*, \quad (8)$$

where  $a_L$  and  $b_L$  are dimensionless empirical constants for which Sklar and Dietrich (2004) found values of  $a_L = 8$  and  $b_L = 0.88$  based on a compiled database of experimental studies. Auel et al. (2017a) reassessed this database and expanded it with later flume studies (Ancy et al., 2002; Chatanantavet et al., 2013) and their own experiments. They found smaller hop lengths  $a_L = 2.3$ , while the scaling factor remained similar,  $b_L = 0.8$ . We use the latter model parameters in this study, which are also consistent with observations by Gimbert et al. (2019); Figure S3-1a in Supporting Information S3), and explore the potential implications of the application of other values.

Similar to hop length, the vertical impact velocity  $u$  of bedload grains can be described as equation 9:

$$u(D) = a_u \sqrt{gsD} \left( \frac{\tau^*}{\tau_c^*} - 1 \right)^{b_u} \text{ for } \tau^* > \tau_c^*. \quad (9)$$

Sklar and Dietrich (2004) estimated a value for impact velocity  $u$  based on relations of hop height, trajectory (ratio rising and falling limb), and descent time, which was rewritten as a function of transport stage by Auel et al. (2017b) with constants  $a_u = 0.84$  and  $b_u = 0.18$ . Direct flume measurements of impact velocity distributions have since then been done in supercritical flow experiments for smooth (Auel et al., 2017b) and rough flow conditions (Gimbert et al., 2019). Gimbert et al. (2019) derived values of  $a_u = 0.51$  and  $b_u = 0.25$  for near-vertical impacts, which we use as model parameters in this study considering the rough nature of the riverbed.

To determine fractional bedload flux with equation 6a, we need the particle impact rate  $J$ , which we can derive from the (total) measured seismic power  $P$  and the modeled power associated with random individual impacts  $P_i$ . We determine  $P_i$  through filling equations 2, 3, and 4 into equation 1, resulting in equation 10:

$$J = P/P_i \approx P(f, r, D) \frac{\rho_s^2 v_p^3 v_g^2}{Z^2 \pi^2 f^3 m^2 u^2} \chi^{-1}(\beta). \quad (10)$$

In the implementation of equation 3, we assume  $\gamma = 2$ , that is perfectly elastic impacts of particles as they travel under water over a consolidated riverbed (these conditions differ from the active drop experiment with a large rock where we assume  $\gamma = 1$ ), conforming to Tsai et al. (2012). Further, we use  $u$  as defined in equation 9 and  $\chi(\beta)$ , which is a function that approximates the amplitude decay of ground vibrations (expressed through the exponential in the Green's function, equation 4) for an infinitely long and straight river observed at a minimum distance  $r$  in equations 11a and 11b (Tsai et al., 2012):

$$\chi(\beta) \approx 2 \ln(1 + \beta^{-1}) e^{-2\beta} + (1 - e^{-\beta}) e^{-\beta} \sqrt{2\pi\beta^{-1}}, \quad (11a)$$

$$\beta = \frac{2\pi r(1 + \xi) f^{1+\xi-\eta}}{K_0 v_p \rho f_0^{\xi-\eta}}. \quad (11b)$$



Finally, to determine bedload flux over a complete particle-size distribution ( $p(D)$ ; Figure 2), we integrate the fractional loads from equation 6a as follows in equation 12:

$$q_b = \int_{D_{min}}^{D_{max}} p\left(D, \frac{\tau^*}{\tau_c^*}\right) q_b(D) dD. \quad (12)$$

We truncate and (re-)normalize the particle-size distribution to consider only those particles that are in motion ( $\tau^* > \tau_c^*$ ), thus accounting for partial transport conditions.

### 3.5. Model Application for Bedload Quantification

#### 3.5.1. Scaling Analysis

Our first assessment of the seismic bedload model is based on a scaling approach where we assess the power-based dependency of seismic power on sampled bedload flux. This gives insight into the coherence of the seismic response (e.g., Burtin et al., 2011) and the contributions of the different sources to the total seismic power (e.g., Roth et al., 2016; Roth et al., 2017). According to Tsai et al. (2012), seismic power due to bedload transport is expected to scale to the power 2 with particle mass,  $P_b \sim m^2$  (equation 10), to scale linearly with bedload flux given a constant particle size,  $P_b \sim q_b D_{94}^3$  (equations 6a and 10) and to scale to the power 6 with particle diameter,  $P_b \sim m^2 \sim D_{94}^6$  (equations 6a and 10), since  $m \sim D^3$  and the dominant particle size is the 94th percentile ( $D_{94}$ ). If we include the effect of particle-size dependency for hop length (equation 7) and impact velocity (equation 8) on bedload flux (equation 6a), the scaling relation becomes  $P_b \sim q_b D_{94}^{3.2} \sim D_{94}^{6.5}$ . To determine scaling relations, we fit the data using major axis regression which takes into account the uncertainties in both the inverted and sampled bedload fluxes. Fitting is performed on the basis of the perpendicular distance of each data point to the regression line rather than the distance along the y-axis as is done in ordinary least squares regression.

In addition, we perform a scaling analysis using the measured flow discharge, where seismic power due to flow turbulence ( $P_w$ ) is expected to scale with discharge as  $P_w \sim Q_w^{1.4}$ , for channels where  $W \gg h$  (Gimbert et al., 2016). This scaling is expected to be manifest at frequencies lower than those characterized by bedload transport (Gimbert et al., 2014). For the scaling with discharge, we use nighttime values, from 22:00 to 06:00, to limit potential effects of anthropogenic background noise (McNamara & Buland, 2004). Indirectly, we can then also address seismic power due to bedload transport ( $P_b$ ) following the bedload rating curve defined for this site by Missot et al. (2020),  $q_b \sim Q_w^{5.3}$ . Because no systematic change in particle size has been observed during the sampling period (Missot et al., 2020), seismic power may be expected to scale linearly with bedload flux and therefore  $P_b \sim Q_w^{5.3}$ .

#### 3.5.2. Bedload Flux Inversion

For the inversion of bedload fluxes, we use the locally derived seismic characterization (section 3.3) and revised formulation of the physically-based bedload transport model (section 3.4; equation 6a). For the latter, we calculate bedload dynamics for the particle-size distribution of the riverbed as determined for the braided reach (Figure 2). Missot et al. (2020) have shown that this reach is an important source of sediment that is exported downstream where similar particle-size distributions were sampled and where we invert bedload transport rates (B1; Figure 1). We visually fitted a log-“raised cosine” distribution, as introduced by Tsai et al. (2012), to the sampled data sets, taking particular care to get an accurate representation of the largest fractions that contribute strongly to the seismic signal (Figure 2). The distribution was discretized with particle fractions  $dD$  of 5 mm, ranging from  $D_{min} = 1.6$  mm to  $D_{max} = 0.44$  m to determine the total load with equation 12. For the particle dynamics, we determine hop length and impact velocity based values for  $\tau^*$  and  $\tau_c^*$  for particles in motion observed at B1, given that the criterion for motion is exceeded in the braided reach source area (Figure 1). This calculation was however conditioned by sediment mobility in the upstream braided reach, where we use the values derived by Missot et al. (2020); appendix A therein.

We compare the inverted bedload fluxes with sampled fluxes derived from Missot et al. (2020). Although we use the sampled loads for the validation of the seismic approach, we would like to emphasize here that direct bedload measurements have a considerable uncertainty (Vericat et al., 2006). For this reason, we employ major axis regression as mentioned earlier. Considering the assumptions and uncertainties associated with both the seismic framework and bedload dynamics, we use a number of scenarios to explore the implications of different plausible parameter sets on inverted bedload flux.

## 4. Results

### 4.1. Experimental Characterization of Riverbed Seismic Response

#### 4.1.1. Seismic Wave Propagation

The seismic waves generated by individual rock impacts on one bank were observed by a geophone on the opposite bank at a distance of more than 100 m (see example Figure 3a). Frequencies for which the impacts could be identified lie in the range of 10–30 Hz. The determined wave group velocities differ little between the upstream and downstream cross section, apart from outliers (symbols without a fill) that are associated with higher-order modes and that we do not consider here. The data are described with a power-law dependency on frequency (Figure 3b), least squares fitting of the function  $v_g = v_{p0}(f/f_0)^{-\xi}/(1+\xi)$  that follows from combining equations 5b and 5c. The observed velocities are within the range (120–920 m/s) found by Huang et al. (2007), using a similar experiment in debris flow channels, but are considerably lower than the reference values provided in Tsai et al. (2012) for generic bedrock sites. We also note that from ~16 Hz, velocities appear to approach a constant value of ~180 m/s, which can be related to the presence of a distinct sedimentary top layer in the subsurface (on the order of one wavelength or ~10 m thick) that has relatively uniform wave propagation. Unlike wave group velocity, wave phase velocity cannot be identified visually and we calculate these with equation 5c using the values  $v_{p0} = 680$  m/s and  $\xi = -0.31$  obtained from Figure 3b.

#### 4.1.2. Attenuation of Seismic Power

Spectrograms of the active drop-experiment show that seismic power associated with rock impacts decays with distance (Figure 4a). At a short range, impacts may be observed over a wide frequency band of 10–70 Hz, but this range becomes narrower, ~15–40 Hz at a distance of 150 m for site R2 (Figure 4b; for spectrograms of sites L1, L2, and R1, see Supporting Information S1). The lower half of this frequency range corresponds to the range for which wave group velocity could be determined. Frequencies around 10 Hz have a higher level of background noise, which is likely to be generated by river flow turbulence (Burtin et al., 2011; Gimbert et al., 2014).

Using the fitted velocity function from Figure 3b and limiting the extrapolated values for high frequencies to 180 m/s (Figure 3b), we derived fitted values for the quality factor  $K$  (Figure S2-1 in Supporting Information S2). The response of seismic power as a function of distance from impact and frequency is well described using the Green's function (equation 4) as shown in Figure 5. Scatter is smallest for the higher frequencies at which seismic power decreases more rapidly with distance. The observed frequency dependency of  $K$  (fitted with equation 5d) is not very strong, which is consistent with the presumed presence of a uniform subsoil. The value approaches 20 (Figure 5 inset), which was used as a constant by Tsai et al. (2012).

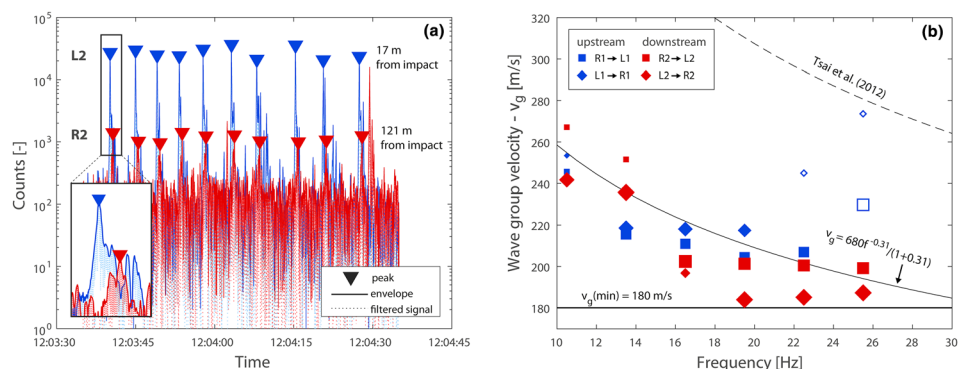


**Figure 3.** (a) Seismogram filtered for frequency (19.5–25.5 Hz in this example) bounded with a signal envelope and identified peak amplitudes corresponding to 10 drops that were performed at 17 m from L2 and 121 m from R2; the inset provides a zoom-in of the first drop. (b) Wave group velocity per filtered frequency range (50% overlapping bins of 6 Hz) between geophones on opposite banks; for example, L1 → R2 indicates the velocity of waves that originate from the impact site closest to L1. Each data point represents the median of 10 drops; the size gives an indication of the confidence based on the standard deviation of the registered time delay between these drops; larger data points indicate a lower standard deviation and vice versa. A regression curve (black) that describes the wave group velocity dispersion curve based on equations 5b and 5c was fitted using all the data, excluding the outliers, shown with no fill, that are associated with higher-order modes.

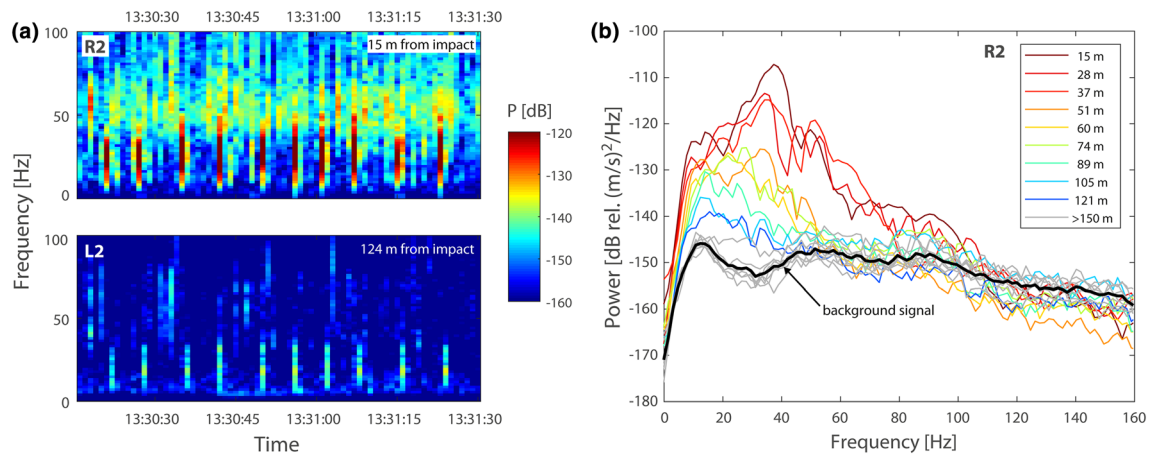


**Figure 4.** (a) Spectrograms of a series of 10 impacts that were performed at 15 m from R2 (top) and 124 m from L2 (bottom). (b) seismic power with distance from rock impact observed with geophone R2; the spectrograms at the time of the impact in panel (a) are represented as a line in panel (b).

### 4.1.3. Seismic Inversion for Large-Rock Impact Experiment

To validate the seismic framework, we invert the mass of the rock used in the active drop-experiment, multiplied with the residual amplitude factor  $Z$ , from the seismic measurements using equations 2 and 3. For the frequency range 12.5–37.5 Hz, in which impacts could be identified, the mass of the rock is well estimated with no evidence of net effects on the seismic amplitude ( $Z = 1$ ; Figure 6). Residual standard deviation among the observations is approximately  $\pm 5$  kg or  $\pm 30\%$  of the known mass. When applying the wave propagation and attenuation parameters suggested by Tsai et al. (2012) as a first estimation, the seismic inversion also gives reasonable values, although there is a frequency-dependent bias in the inverted mass. For lower frequencies, the application of these parameters may lead to an overestimation of a factor 2–3, but at higher frequencies, this error is marginal.

These results not only demonstrate that the seismic framework is applicable in a gravel-bed river setting but also highlight the need to locally derive the constituent parameters of the Green's function. We have shown that this may be accomplished with a simple active experiment. To be able to invert bedload fluxes at site B1, we used an additional small-scale drop experiment to verify the application of the calibrated Green's function and the presence of any local site amplification at B1.

The resulting  $Z$  values (Figure 6 inset) indicate that the seismic framework can be applied quantitatively, with the note that at 12.5 Hz there is an apparent site amplification effect.

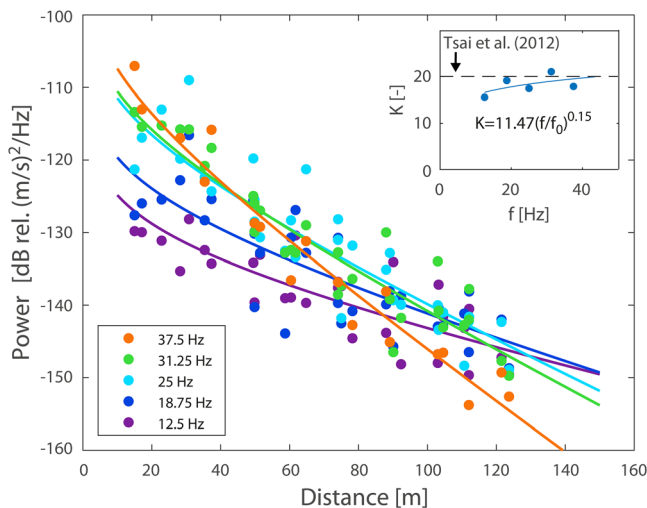


**Figure 5.** Seismic power decay with distance per frequency following the expression of the Green's function (equation 4). The inset shows the quality factor  $K$  derived from fitting normalized power based on the Green's function (see Supporting Information S2).

## 4.2. Continuous Bedload Quantification From Seismic Measurements

### 4.2.1. Seismic Power Scaling Relationships

Seismic power shows frequency-based power-law scaling with bedload transport (Figure 7a; exponent is the slope in log-space). At 50 Hz, the scaling is approximately linear (exponent  $\approx 1$ ), which is consistent with predictions from Tsai et al. (2012) for bedload-induced seismic vibrations, assuming a constant particle size distribution. Bedload still appears to dominate the signal at 30 Hz, as the scaling exponent is only slightly lower than 1, but this is no longer the case at 10 Hz where the exponent of the power-law is much smaller. Note that the use of major-axis regression, which also accounts for uncertainties in the bedload sampling, leads to considerably higher regression slopes than ordinary least squares regression (exponents of 0.24, 0.71, and 0.78 for 10, 30, and 50 Hz, respectively). The data appear to show an increase in scatter with increased seismic power and there is a potential flattening-off in the data of 30 and 50 Hz from approximately  $10 \log_{10} q_b = -8$  (the 10 largest sampled  $q_b$  values fall below the regression line).

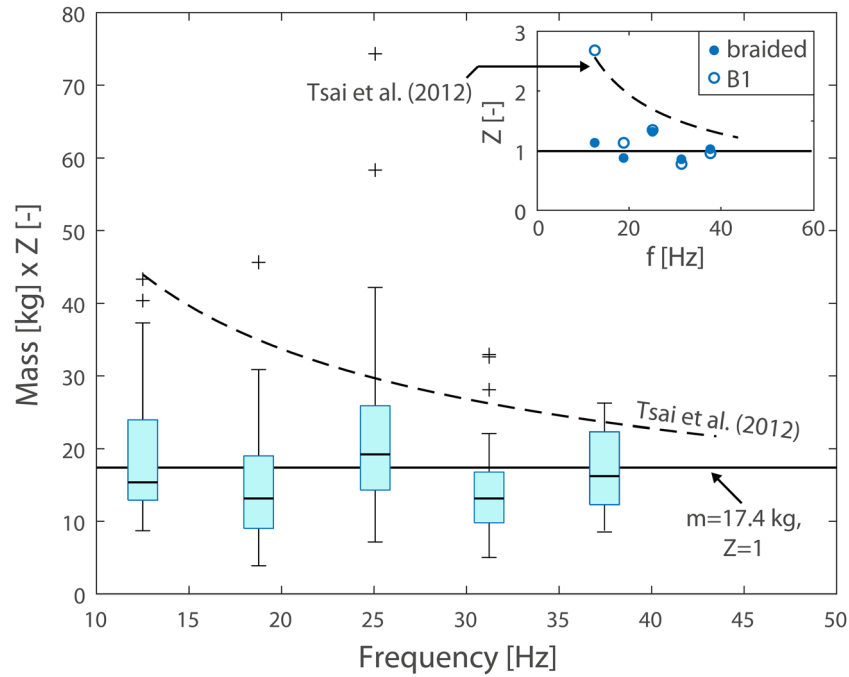


**Figure 6.** Inverted mass multiplied with the net amplification factor ( $Z$ ) plotted against frequency for the active drop-experiment. The known rock mass is shown assuming  $Z = 1$ , while the dashed line is derived based on first-estimate parameters in Tsai et al. (2012). The boxes give the range of data per frequency that lies between the 25th and 75th percentile within the boxes horizontal lines that mark the median value; the whiskers covers the range without outliers (0.7 and 99.3 percentile), and the outliers are marked as +. The inset shows the  $Z$  values per frequency for the braided river reach and at site B1. Here, we also derived  $Z$  values that would be required to obtain the prescribed mass using the set of Green's function parameters given in Tsai et al. (2012).

When we account for sample-dependent particle size, the scatter around the scaling relation with bedload transport improves in terms of an increase in Spearman's  $r$  value (we use Spearman's rank correlation because of the nonlinear axes) and a decrease in the median residual from a factor  $1.2^{\pm 1}$  to  $1.1^{\pm 1}$  for 30 and 50 Hz (Figure 7b). Despite uncertainties associated with the small data set (for this reason, we fixed the exponent of the regression based on Figure 7a) and limited range in particle size that is caught during sampling, this result indicates that particle size dynamics may account for a significant part of the residual seismic variability in Figure 7a and supports the physical basis of the applied bedload transport model. Of

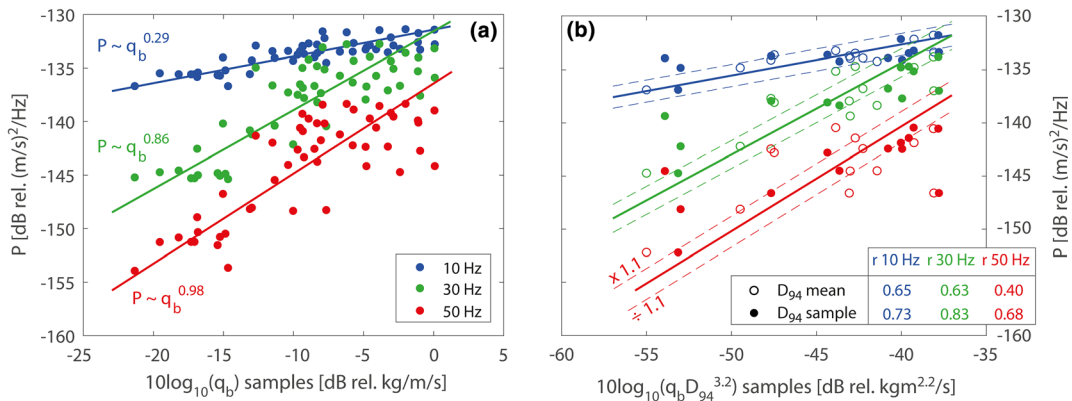


**Figure 7.** (a) Seismic power for 10, 30, and 50 Hz against bedload flux scaled as a  $10\log_{10}$  value to match the dB scale of the seismic power; major axis regression lines describe the power relations per frequency. (b) Seismic power for 10, 30, and 50 Hz against bedload flux multiplied by  $D_{94}^{3.2}$  ( $10\log_{10}$  scaling) for the samples for which particle size was determined (13 of the 51 samples in panel (a) for which seismic measurements were available). For these samples, the values are plotted using both the mean particle size and the sample-specific measured particle size which leads to increased Spearman's  $r$  values (shown in the legend). The major axis regression line is fit to the data, given the exponents derived in panel (a), and offsets of a factor  $1.1^{\pm 1}$  perpendicular from these regression lines are provided as a reference.

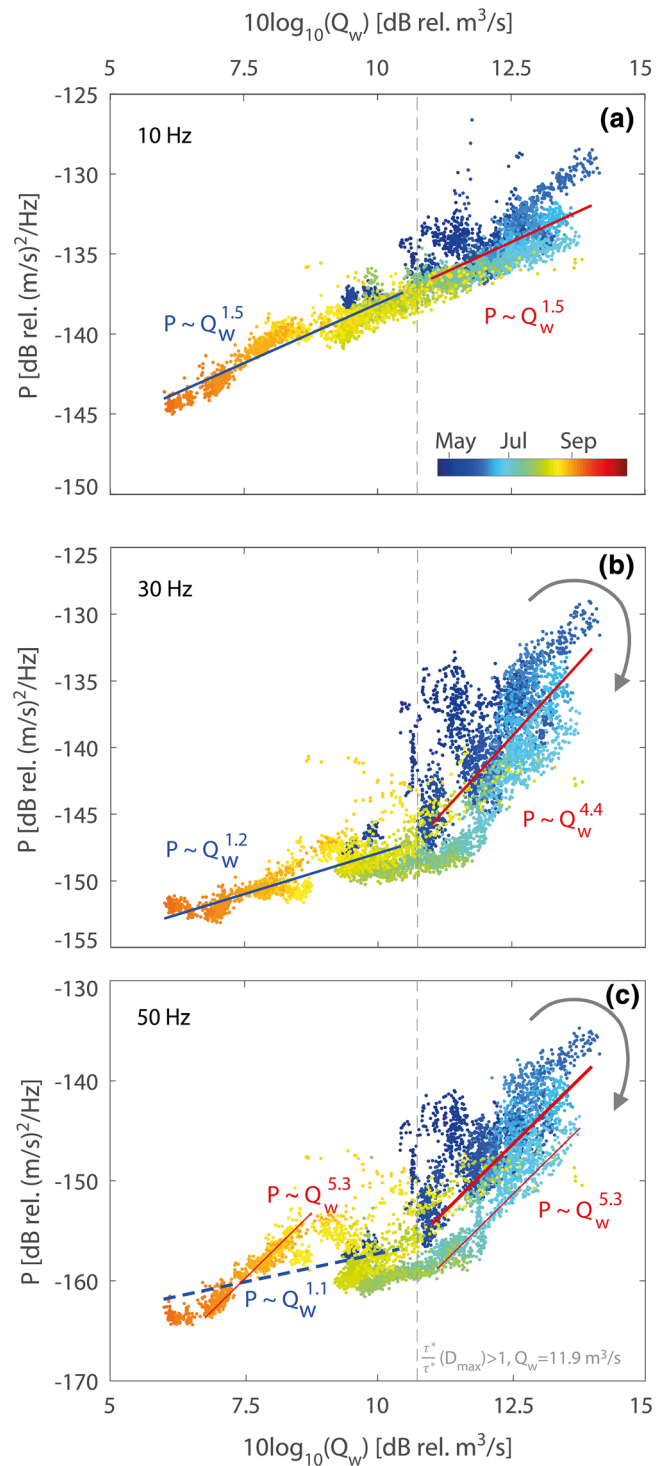


**Figure 8.** Plots of seismic power per frequency 10 Hz (a), 30 Hz (b), and 50 Hz (c) against discharge scaled as a  $10\log_{10}$  value to match the dB scale of the seismic power. Data are shown for the whole season (color scale indicating months). Least squares regression lines describe the seismic power for discharge above and below the modeled threshold of full particle mobility,  $\tau^*/\tau_c^*(D_{max}) > 1$  at  $Q_w = 11.9 \text{ m}^3/\text{s}$ , where there is an apparent change between a turbulence-dominated and bedload-dominated seismic signal. For panel (c), the line below threshold is dashed due to poor fit, and we added two additional lines where  $P \sim Q_w^{5.3}$  as a reference to indicate different phases with ample sediment supply and partial bedload transport. Note that the limits of the y-axes differ.

course, strong deviations may still be expected due methodological limitations to resolve the temporal and spatial variability in bedload flux.

We can indirectly verify the bedload sample scaling relationships with those obtained with discharge (Figure 8). At a low frequency of 10 Hz, the power-law scaling can be described with a continuous function with an exponent of 1.5 (Figure 8a; note we use least squares regression here as the uncertainty in discharge is negligible) that is very close to the value of 1.4 expected based on the physical modeling of turbulent flow (Gimbert et al., 2016). It does not mean that no bedload transport occurs, but rather that at such a low frequency, bedload-induced ground vibrations are overwhelmed by vibrations due to flow turbulence. Because flow turbulence drives bedload transport, we find a clear scaling relation with sampled rates at 10 Hz in Figure 7 but, due to the nonlinear nature of bedload transport with discharge, with a lower exponent value.

At 30 and 50 Hz, a clear change in scaling power occurs as discharge exceeds a value ( $11.9 \text{ m}^3/\text{s}$ ) that corresponds to the modeled threshold of full particle mobility (Figure 8b, 8c) and can be related to pavement breakup in the braided reach as observed here by Missét et al. (2019). For discharges higher than this critical value, the power-law trend is steeper with an exponent of 4.4 at 30 Hz and 5.3 for 50 Hz. The latter corresponds to the  $q_b \sim Q_w^{5.3}$  rating curve found by Missét et al. (2020) under the condition that  $P_w \sim q_b$  as predicted by Tsai et al. (2012). The trend also describes a more scattered data set that exhibits a clockwise hysteresis in May–July (note that the hysteresis may also be detected at 10 Hz in Figure 8a although it is clearly less pronounced). The wider scatter is similar to the plot with sampled load (Figure 7a), but in this case, there is no evidence of signal saturation. For discharges lower than the identified threshold, mainly in August–September when little to no bedload transport was observed, the trend is similar to that for 10 Hz, although slightly lower exponents are found. For 50 Hz, the lower discharges ( $<11.9 \text{ m}^3/\text{s}$ ) now exhibit a baseline response, which still has a power scaling of just more than 1, but also shows a period with a steeper response (indicated by a thin red line with exponent 5.3). The latter follows directly after a large flood on 9 August (peak flow  $\sim 45 \text{ m}^3/\text{s}$ ), which temporarily led to low rates of partial transport that are not visible at lower frequencies due to the dominant effect of flow turbulence (note the differences in the y-axis limits in Figures 8a to 8c). This period of transport may be associated with changes in channel morphology and sediment availability, that is, the reworking of channel-lag deposits after the flood. Periods of increased sediment supply and associated changes in critical discharge may therefore be observed, while the characteristic bedload scaling relationship remains constant.

The results of the scaling analysis are summarized in Figure 9, showing both the exponent (a) and the Spearman's  $r$  value of the relationship (b). For the lower discharges, we see a clear scaling of 1.4 with discharge ( $r > 0.8$ ) for frequencies up to  $\sim 15$  Hz, which is in agreement with Gimbert et al. (2014). At higher frequencies, this scaling weakens as bedload transport becomes dominant as indicated by the exponent (Figure 9a). Due to hysteresis, the frequency range for bedload cannot be solely identified on the basis of the  $r$  value (little variation with frequency in Figure 9b), as is the case for the frequency range for turbulence. The scaling of seismic power against discharges for which full particle mobility is expected on one hand and the scaling of seismic power against sampled bedload flux on the other hand are remarkably similar and in agreement with Tsai et al. (2012). They both increase between 15 and 30 Hz, indicating a transition from a flow turbulence-dominated to a bedload-dominated seismic signal. Although the discharge relation is slightly less strong, it provides a good control and potential alternative for the bedload flux scaling. The range of frequencies for which bedload may be inverted is 30–70 Hz, above which the exponents of the scaling relations ( $Q_w > 11.9$  and  $q_b$ ) rapidly decrease and become much smaller than the expected values (1 and 5.3, respectively) for bedload transport.

#### 4.2.2. Bedload Flux Inversion From the Seismic Record

When applying the physically-based bedload model, using locally derived seismic, hydraulic, and particle size parameters, we invert transport rates from measured seismic power for different frequencies (Figure 10). The results show that the seismically derived values for frequencies in the range of  $\sim 30$ –50 Hz correspond well to those derived from instream sampling ( $q_b(P) \approx q_b$ ) across the full range of transport rates from less than 0.01 to nearly 1 kg/m/s. The data scale nearly linearly against each other (as seen earlier in Figure 7a assuming a single particle size and not a discharge-dependent distribution) and the magnitude of the inverted values is also in good agreement with the independently obtained bedload samples. Most

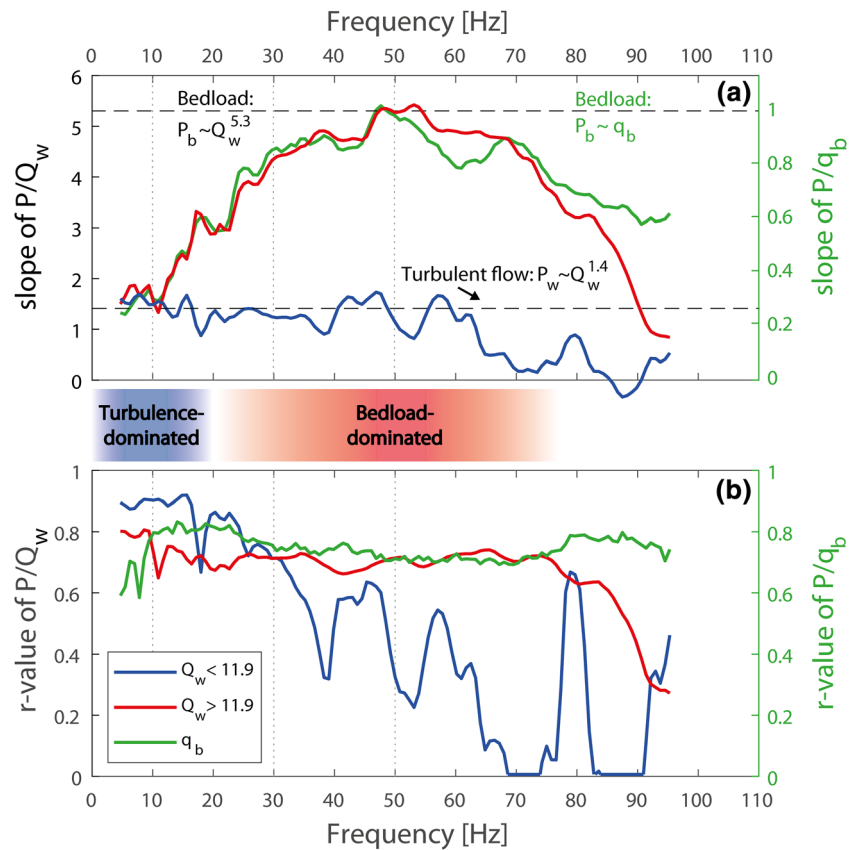


**Figure 9.** Characterization of seismic power per frequency for discharges above and below  $Q_w=11.9 \text{ m}^3/\text{s}$ , the estimated threshold of full particle mobility. (a) Power of the scaling relation, slope of  $P/Q_w$  and  $P/q_b$  (discharge on the left axis and bedload flux on the right axis) on a log-log scale as in Figures 7 and 8. Dashed lines indicate predicted scaling values for bedload and turbulent flow as predicted based on the physically-based models of Tsai et al. (2012) and Gimbert et al. (2014) respectively. (b) Spearman's  $r$  values associated with the scaling relations. Thin vertical lines in panels (a) and (b) indicate the frequencies 10, 30, and 50 Hz.

instantaneous values fall within a factor of  $5^{\pm 1}$  (i.e., between 0.2 and 5), while the regression lines lie within a factor of  $\sim 2^{\pm 1}$ ; the regression line of 50 Hz shows negligible error. Only for 25 Hz, there is markedly lower exponent and general overprediction of bedload rates, which may be directly attributed to flow turbulence that significantly affects the seismic signal at these low frequencies (Figure 9a). Although seismic power scales with bedload flux up to frequencies of 70 Hz (Figure 9a), we limit the quantitative inversion to 50 Hz due to the uncertainties associated with the extrapolation of the results of the seismic characterization (Figure 6).

#### 4.2.3. Modeling Sensitivity and Uncertainty

Although we have applied the modeling to local conditions, there remain uncertainties in the seismic characterization (wave propagation and attenuation) and assumptions concerning (modeled) bedload dynamics. These uncertainties may propagate into the inverted bedload fluxes as illustrated for a number of plausible scenarios in Table 1.

In Scenario 1, we use the first-estimate seismic parameter values for  $v_g$ ,  $v_p$ , and  $K$  that were provided by Tsai et al. (2012) to quantify the relevance of the active drop-experiment on bedload fluxes. The derived bedload rates are systematically higher than those from the applied model with the largest differences occurring at low frequencies, a factor of nearly 4 at 31.25 Hz (2.03 vs 0.55 for factor  $a$  in Table 1). Note that the relative difference in inverted transport rates is larger than that of the inverted masses of a single rock at this frequency (factor  $\sim 1.5$  in Figure 6). This is because, for a given seismic power, the apparent error in the active experiment in terms of  $Z^{-1}$  scales linearly with force (equation 2) and thus mass (equation 3), while in the

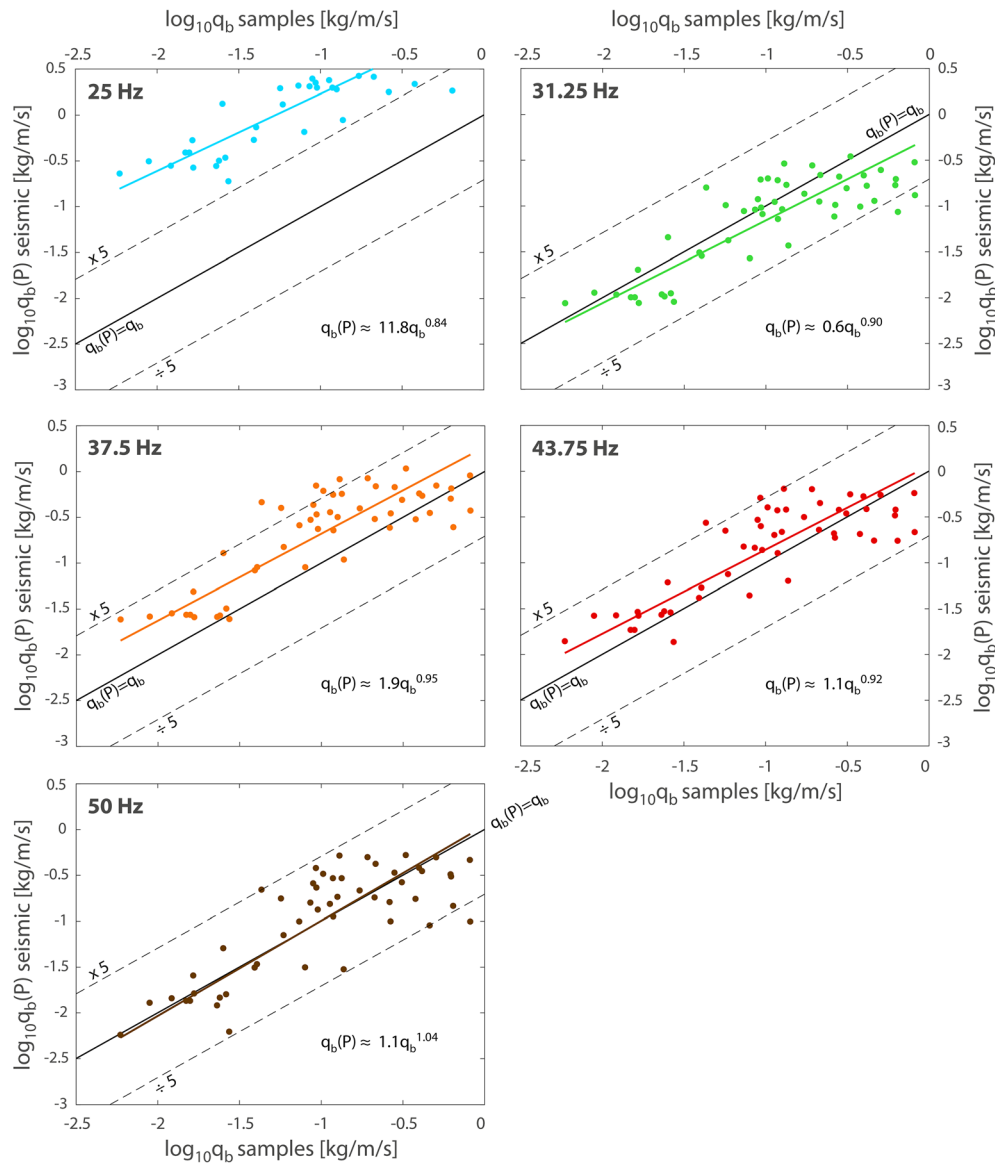


**Figure 10.** Double-logarithmic plots of bedload transport rates derived from seismic power  $q_b(P)$  using the physically-based model compared to sampled loads  $q_b$  per frequency. The power-law relations were derived using major-axis regression; lines indicating  $q_b(P) = q_b$  and offsets of a factor  $5^{\pm 1}$  perpendicular from the regression line are provided as a reference. Note that not all data points are shown for 25 Hz (the limits of the y-axes are the same for all plots) and that the regression line of 50 Hz lies more or less on the line  $q_b(P) = q_b$ .

case of bedload flux, for a given power and particle size,  $Z^{-2}$  scales with impact rate (equation 10) and bedload flux (equation 6a). The nonlinear propagation of  $Z$  makes it important to obtain a good field constraint on its (effective) value.

In Scenario 2 (Table 1), we use the detailed description of bedload dynamics following Tsai et al. (2012) while using the seismic parameters as derived in this study. The results vary slightly from those of Scenario 3, where we simplified the bedload dynamics through assessing hop length and impact velocity directly based on transport stage (see Figure S3-1 in Supporting Information S3 for a comparison of the  $L$  and  $u$  values) even through the underlying database on which the empirical formulations are based is the same. For both Scenarios 2 and 3, the exponent  $b$  of the regression is larger than in the applied model (0.94 and 0.95 vs. 0.90; Table 1). In Scenario 4, we use the values derived for  $L$  and  $u$  by Auel et al. (2017a, 2017b) for flow conditions over a fixed planar bed, which leads to much higher (order of magnitude) estimates of bedload transport due



**Table 1**

Sensitivity Analysis of Bedload Inversion for 31.25 and 50 Hz Based On the Factor  $a$  and Exponent  $b$  of the Regression Function  $q_b(P) \approx aq_b^b$

Frequency (Hz) scenario	Factor $a$ : $q_b(P) \approx a q_b^b$		Exponent $b$ : $q_b(P) \approx a q_b^b$	
	31.25	50	31.25	50
Applied model in Figure 10	0.55	1.10	0.90	1.04
1. $v_g$ , $v_p$ , and $K$ from Tsai et al. (2012)	2.03	1.80	0.90	1.04
2. Bedload dynamics from Tsai et al. (2012)	0.59	1.18	0.94	1.07
3. $L$ and $u$ based on S&D (2004)	0.71	1.42	0.95	1.08
4. $L$ and $u$ based on Auel et al. (2017a, 2017b)	14.38	28.54	0.85	0.98
5. Critical shear stress $\tau_{c50}^* = 0.03$	0.70	1.39	0.88	1.02
6. Critical shear stress $\tau_{c50}^* = 0.065$	0.31	0.60	0.65	0.76
7. Particle size $D-1$ cm	101.78	202.14	0.89	1.02
8. Particle size $D+1$ cm	0.14	0.28	0.91	1.05

Note. The parameterization of the applied model is described in section 3, and the values of  $a$  and  $b$  correspond with the results in Figure 10. For the alternative Scenarios 1–8, see the main text. S&D (2004) is a shorthand reference to Sklar and Dietrich (2004).

to a reduced impact velocity (Figure S3–1). In Scenarios 5 and 6, uncertainties regarding the value of the dimensionless critical shear stress (e.g., Buffington & Montgomery, 1997; Recking, 2009) are explored through the use of respectively lower and higher values that may occur in this type of setting (in the applied model  $\tau_{cD_{50}}^* = 0.047$ ), which may have a large impact on the exponent of the regression due to changes in the particle-size distribution that is in motion. In Scenario 6, the particle distribution effectively becomes finer at low discharges due to the increased critical shear stress, resulting in a higher bedload flux to account for the generated ground vibrations. A change in particle-size distribution may occur due to upstream changes in sediment sources (e.g., sediment delivery from a debris flow). A general fining of  $-1$  cm in Scenario 7 will lead to a large overestimation of the bedload flux of  $\sim 2$  orders of magnitude. Conversely, in Scenario 8, the coarsening of the entire particle-size distribution ( $+1$  cm) leads to an underestimation of the bedload flux (order of magnitude) that may account for the generated ground vibrations. These findings illustrate that the particle-size distribution is a key factor in the applied model (Tsai et al., 2012) and needs to be well constrained in the field.

## 5. Discussion

### 5.1. Constraining Seismic Parameters From Rock Impact Force

In this study, we consider the application of a seismic framework through performing a simple active drop-experiment to characterize seismic wave propagation and attenuation in a braided riverbed. Using geophones on opposite riverbanks, we quantified wave group velocity,  $\sim 200$  m/s at 25 Hz, which is commensurate with values found in debris flow channels (Huang et al., 2007). The velocities are however markedly lower than those in generic bedrock settings (Boore & Joyner, 1997) which have been used as a first estimation in Tsai et al. (2012). Rayleigh waves appear to exhibit little dispersion in this riverbed setting at the frequencies of interest ( $>20$  Hz; Figure 3b) and it may therefore be justified to assume a constant velocity due to the wave propagation through a relatively shallow and uniform sediment layer. Using a Green's function, we could approximate the frequency-dependent decay of wave amplitude with distance and derive the quality factor  $K$  of the subsurface, which is close to 20 (Figure 5a) and in line with the value used by Tsai et al. (2012). Most importantly, we show that the relatively simple experimental design and the (semi-)empiric nature of the seismic framework can adequately describe both seismic wave propagation (Figure 3b) and wave attenuation in the riverbed (Figure 5b). The difference in the spatial decay of seismic power at frequencies dominated by flow turbulence and bedload transport, as dictated by the Green's function parameters, may be used to determine a suitable distance from the river to monitor bedload (see Gimbert et al., 2014). Although the obtained wave velocity and quality factor  $K$  may be indicative for this type of gravel-bed river setting, we strongly recommend local derivation of the interdependent seismic parameters (Morozov, 2010) that may vary to a large extent due to the spatially variable nature of the subsurface (e.g., Huang et al., 2007).

In a field setting, it is critical to assess the absolute amplitude of the seismic signal as any residual error will affect inverted bedload transport rates in a nonlinear fashion (scenario 1 and 2; Table 1). Based on the active

experiment across the braided reach, we found no significant amplification effect (Figure 6) and we could accurately invert the mass of the rock used in the active drop-experiment from seismic measurements for a range of frequencies (~15–40 Hz) with a standard deviation of approximately  $\pm 5$  kg or  $\pm 30\%$ . The experiment and analyses we present may be a simple yet important means to quantify seismic response and to constrain the seismic power associated with bedload transport.

## 5.2. Quantifying Bedload Flux Using a Physically-Based Bedload Model

In this study, we show the presence of a pronounced bedload signal in seismic power records that scales nearly linearly with bedload flux in the range of ~30–50 Hz (Figure 7a, Figure 9), which is in agreement with the theoretical model of Tsai et al. (2012). Particle size variability may account for significant scatter in this scaling relationship (Figure 7b), supporting the physical basis of the bedload model we used and, at the same time, showing its sensitivity to this parameter. To complement punctual bedload measurements, we show that a scaling approach of seismic power with continuous discharge measurements allows the frequency range dominated by bedload to be clearly constrained (Figure 8), which is crucial for the accuracy of subsequent bedload transport inversions. We confirm the applicability of the power scaling from the theoretical model of Gimbert et al. (2014, 2016),  $P_w \sim Q_w^{1.4}$  for 5–15 Hz, and use this together with an established bedload rating curve (1) to verify the linear bedload scaling on a continuous scale, which allows the inversion of variable loads and giving confidence in the extrapolation to higher loads and (2) to assess the onset and magnitude of bedload transport (Figure 8) which vary with temporal changes in the transport and supply dynamics associated with morphological changes in the upstream braided reach (Misset et al., 2020). The scaling analysis allows the underlying processes to be distinguished based on causality, something that may not be possible with statistical techniques alone. In particular, the highest  $r$  value in Figure 9b for  $q_b$  is found at 15 Hz, which is dominated by flow turbulence rather than bedload. This illustrates that empirical fitting and optimization approaches (e.g., Dietze et al., 2019; Roth et al., 2016) require careful application as they are susceptible to error and misunderstanding. The scaling analysis we present here will help to further investigate bedload processes that have been inferred from event to seasonal-based hysteresis patterns (Barrière, Oth, et al., 2015; Burtin et al., 2008; Hsu et al., 2011; Roth et al., 2014).

Through considering and quantifying seismic attenuation and potential amplification effects (Figure 6) in the subsurface, we could accurately invert bedload fluxes from measured seismic power. The values correspond to independently sampled bedload fluxes, with uncertainties generally within a factor of  $5^{\pm 1}$ , while the measurements themselves span 2–3 orders of magnitude (Figure 10). This is not much more than the factor  $2^{\pm 1}$  derived in a controlled flume setting by Gimbert et al. (2019). Our results are encouraging considering the inherent uncertainties associated with both seismic and sampling techniques (Tsai et al., 2012; Vericat et al., 2006) and the natural variability in bedload transport (e.g., Gomez et al., 1989) and associated particle size (Figure 7b; Misset et al., 2020). When temporal fluctuations are averaged out, the continuous seismically derived bedload fluxes may be expected to have an uncertainty of  $\sim 2^{\pm 1}$  (deviation regression lines in Figure 10). Based on scenario calculations (Table 1), we illustrate the sensitivity and uncertainty of the bedload inversion results which we cannot directly evaluate with sampled loads, stressing the importance of local seismic characterization and a physically-based modeling approach.

Our modeling approach, using particle hop length and impact rate as a function of transport stage, is simpler and may be expected to be more accurate than the approach used in Tsai et al. (2012) since no prior assumptions are made on the detailed particle dynamics, that is, the values of parameters  $U_b$ ,  $h_b$ ,  $c_a$ , and  $u_s$ . The resulting differences in parameter values (Figure S3-1 in Supporting Information S3) and inverted bedload fluxes (Table 1) are limited. More importantly, we show that relations for hop length and particularly impact velocity (Figure S3-1) may differ with hydraulic morphological conditions, leading to deviations in inverted bedload fluxes of more than an order of magnitude (Scenario 4; Table 1). Using the more generic model, we profit from recent additions to existing data sets which have led to revised empirical relationships such as for hop length (Auel et al., 2017a) and new measurement methods, for example, smart rocks (Gimbert et al., 2019). The latter allows impact velocity to be measured directly rather than being estimated indirectly. The use of these parameters entails an inevitable uncertainty together with uncertainties due to assumptions regarding the mechanics of bedload transport, for example, the uniform saltation, not rolling or sliding, of particles (Tsai et al., 2012), which may not necessarily be fully satisfied. Our results indicate, however, that

the net effect of these uncertainties has a relatively limited effect on the precision and accuracy of inverted bedload rates.

To successfully monitor bedload dynamics with seismic techniques, it is most important to have a good constraint on particle size, that is, which particles are available and which particles are in transport? This is critical as the (natural) variability in bedload particle size that is supplied and transported may translate to significant errors in bedload rates, particularly on short time scales. Nonlinear effects of the threshold of motion and supply-driven changes in particle size distribution may even lead to systematic, order(s) of magnitude errors in bedload flux (Scenarios 5–8; Table 1). In an attempt to overcome this uncertainty, particle size dynamics may be constrained through the choice of a suitable field setting. First, a measurement site should ideally have a well-known source of (coarse) bedload material; in our case, material is released from the upstream braided reach (Figure 2). Second, supply-limited conditions at a monitoring site typically allow for a constant distribution of fully mobile, saltating particles that are independent of discharge as shown by Misset et al. (2020) in our case. These conditions may also limit potential energy dissipation effects at the bed surface due to unconsolidated bed material (Bachelet et al., 2018; Schmandt et al., 2017; Turowski & Bloem, 2016). Third, seismic monitoring at measurement sites that are instrumented with impact plates or acoustic sensors may provide information on temporal particle size dynamics (e.g., Barrière, Krein, et al., 2015; Mao et al., 2016; Wyss et al., 2016). More generally, an integrated approach where seismic measurements are combined with complementary (direct or indirect) monitoring techniques will provide further insight in quantitative bedload dynamics and how they are reflected in the measurements (e.g., Habersack et al., 2017; Misset et al., 2020). For longer-term (seasonal to decadal) investigations into sediment fluxes and the mechanisms that drive these in fluvial and Alpine environments (e.g., river management or climate change), well-constrained seismic measurements can be readily applied to quantify order of magnitude bedload transport where complementary monitoring is not required or not possible due to limitations of instream techniques.

## 6. Conclusions

To the best of our knowledge, we present here the first comprehensive field validation of the physically-based bedload transport model of Tsai et al. (2012) with independently sampled measurements. A two-step approach is used to evaluate the applicability of various model assumptions, (semi-)empiric relations, and proposed parameter values that underlie (1) the seismic framework and (2) the physically-based bedload saltation modeling.

First, we show that a simple but adequate experiment with a series of large-rock impacts allows the characterization of riverbed surface wave propagation and attenuation using seismic measurements from bank-side geophones. Based on this characterization, rock mass and its impact force can be accurately inverted from seismic power with a standard deviation of approximately  $\pm 30\%$  for the frequency range 15–40 Hz. Using first estimate parameters from Tsai et al. (2012), there is a residual frequency-based bias in the inverted mass of a factor of  $\sim 1.5$ , but perhaps more importantly, the presence of potential site-amplification effects can be verified which may lead to larger errors. Our results confirm the suitability of the seismic framework, that is, a Green's function with locally derived parameters, which is a prerequisite for the quantitative seismic monitoring of bedload transport but also other processes such as subglacial flow (Gimbert et al., 2016) or debris flows (Kean et al., 2015; Lai et al., 2018).

Second, we clearly distinguish turbulent flow and bedload transport sources in seismic measurements using scaling relationships based on the physical models of Gimbert et al. (2014) and Tsai et al. (2012). This provides insights into the transport and supply dynamics associated with braided riverbed morphological changes and allows the bedload signal to be constrained for quantitative inversion. Using a revised formulation of the bedload saltation model proposed by Tsai et al. (2012), we inverted continuous bedload fluxes over a range of transport rates (between 0.01 and 1 kg/m/s), which are in good agreement with estimated fluxes from bedload sampling. The uncertainties are generally within a factor of  $5^{\pm 1}$  for instantaneous measurements but are expected to be even smaller,  $\sim 2^{\pm 1}$ , for longer duration continuous measurements, used in sediment budget studies, for example. To remain within these uncertainties, it is crucial to (1) isolate bedload-generated seismic power from that generated by flow turbulence, or for that matter any other noise source, through discharge scaling analysis and/or the modeling of turbulence effects; (2) to constrain the available and mobile

particle-size distribution through sampling bedload and sediment sources, the latter which requires insight into system-based sediment storage and transfer; and (3) to consider particle dynamics, hop length, and particularly impact velocity that depend on reach hydromorphological conditions.

In this study, we demonstrate that a relatively simple seismic approach can be used to accurately quantify bedload transport rates in gravel-bed streams. Active experiments and seismic power scaling with discharge are indispensable techniques that complement instream calibration measurements (e.g., sampling), making the latter no longer strictly necessary, for example, in inaccessible or hazardous sites. Continuous seismic measurements may be readily used to investigate bedload dynamics, its interaction with riverbed morphological changes, and their combined impact on bedload transfer in Alpine streams.

### Notation

$a_L$	dimensionless factor used to quantify particle hop length based on transport stage
$a_u$	dimensionless factor used to quantify particle impact velocity based on transport stage
$b_L$	dimensionless power used to quantify particle hop length based on transport stage
$b_u$	dimensionless power used to quantify particle impact velocity based on transport stage
$c_a$	dimensionless factor that accounts for the ascent time during particle saltation; $c_a = 0.66$ , see Tsai et al. (2012)
$D$	particle size diameter (m)
$f$	wave frequency (Hz)
$f_0$	wave frequency of 1 Hz
$F$	impact force ( $\text{kgm/s}^2$ )
$g$	acceleration due to gravity; $g = 9.81 \text{ m/s}^2$
$G$	displacement Green's function that describes the frequency and distance-dependent attenuation of power ( $\text{s}^2/\text{kg}$ )
$h$	flow depth (m)
$h_b$	mean height of the bedload layer (m), see Tsai et al. (2012)
$h_i$	height above the surface from which a particle is released before impact (m)
$J$	particle impact rate per unit channel length ( $\text{m}^{-1}\text{s}^{-1}$ )
$k$	angular wavenumber ( $\text{rad/m}$ )
$K$	dimensionless quality factor that describes the nonelastic transfer of energy
$L$	saltation hop length (m)
$m$	particle mass (kg)
$N$	dimensionless amplitude coefficient in the Green's function
$pD$	probability of particle fraction $dD$ ( $\text{m}^{-1}$ )
$P$	Seismic power ( $[\text{m/s}]^2/\text{Hz}$ ). For definition, see equation (1). In figures, values are often given in decibel (dB) relative to $[\text{m/s}]^2/\text{Hz}$ (log-scale)
$P_b$	seismic power due to bedload transport ( $[\text{m/s}]^2/\text{Hz}$ )
$P_i$	modeled seismic power associated with random individual impacts ( $[\text{m/s}]^2/\text{Hz}$ )
$P_w$	seismic power due to flow turbulence ( $[\text{m/s}]^2/\text{Hz}$ )
$q_b$	bedload flux per meter width ( $\text{kg/m/s}$ )
$Q_w$	flow discharge ( $\text{m}^3/\text{s}$ )
$r$	radial distance from the impact source (m)
$s$	submerged specific density of the bedload material; $s = 1.65$
$S$	riverbed slope (m/m)
$t$	time (s)
$T$	time window Fourier transform and temporal resolution of $P$
$u$	particle impact velocity (m/s)
$u_s$	mean particle settling velocity through the bedload layer (m/s), see Tsai et al. (2012)
$U$	flow velocity (m/s)
$U_b$	mean particle velocity parallel to the bed surface (m/s), see Tsai et al. (2012)
$v_g$	wave group velocity (m/s)
$v_p$	wave phase velocity (m/s)
$v_{p0}$	wave phase velocity (m/s) at $f_0 = 1 \text{ Hz}$

$W$	channel width (m)
$V$	vertical ground velocity (m/s)
$Z$	dimensionless amplification factor
$\beta$	function that approximates the inelastic attenuation of seismic power from an infinitely long river
$\gamma$	dimensionless impact elasticity factor; $\gamma = 1$ is perfectly inelastic and $\gamma = 2$ is perfectly elastic
$\eta$	dimensionless exponent used for the dependency of the quality factor on wave frequency
$\lambda$	wavelength (m)
$\xi$	dimensionless exponent used to quantify the dependency of the wave phase velocity on wave frequency
$\rho_s$	bedload particle density; 2,650 kg/m <sup>3</sup>
$\rho_w$	water density; 1,000 kg/m <sup>3</sup>
$\tau^*$	dimensionless shear stress at the bed surface
$\tau_c^*$	dimensionless critical shear stress required for particle entrainment
$\chi(\beta)$	function that approximates the two-dimensional spreading and attenuation of seismic power from an infinitely long river

### Acknowledgments

This work had been conducted within the context of the SNSF fellowship granted to Maarten Bakker (Project P2LAP2\_181420) and the ANR project SEISMORIV granted to Florent Gimbert (Project ANR-17-CE01-0008). Complementary support and field equipment were provided by EDF. Nathan Philippot and Arthur Leclerc performed preliminary data analysis, and Nathan Bodereau, Nathan Valsangkar, and Lucas Montbonnet provided assistance in the field (coordinated by INRAE). We thank Associate Editor Kate Allstadt, Fabian Walter, and two anonymous reviewers for their thoughtful and thorough comments on the initial manuscript. Seismic and discharge data are available at 10-min resolution in Supporting Information S4 and accompanying file “Bakker\_etal\_JGR\_data.xlsx” with this paper, and are available on Mendeley Data (<https://doi.org/10.17632/k6y3ndgv8.1>). Bedload sampling data and riverbed particle size data are provided in Supplementary Materials B and C in Misset et al. (2020), and are available on Mendeley Data (<https://doi.org/10.17632/p57skxcw8b.1>).

### References

- Abbott, J. E., & Francis, J. R. D. (1977). Saltation and suspension trajectories of solid grains in a water stream. *Philosophical Transactions of the Royal Society of London. Series A, Mathematical and Physical Sciences*, 284(1321), 225–254. <https://doi.org/10.1098/rsta.1977.0009>
- Aki, K., & Richards, P. G. (2002). *Quantitative seismology*. Sausalito, Calif: University Science Books.
- Ancey, C., Bigillon, F., Frey, P., Lanier, J., & Ducret, R. (2002). Saltating motion of a bead in a rapid water stream. *Physical Review E*, 66(3), 036306.
- Anderson, J. G., & Hough, S. E. (1984). A model for the shape of the Fourier amplitude spectrum of acceleration at high frequencies. *Bulletin of the Seismological Society of America*, 74(5), 1969–1993.
- Ashmore, P., & Church, M. (1998). *Sediment transport and river morphology: A paradigm for study* (pp. 115–148). Highlands Ranch, Colorado: Water Resources Publications LLC.
- Ashmore, P. E. (1991). Channel morphology and bed load pulses in braided, gravel-bed streams. *Geografiska Annaler. Series A. Physical Geography*, 73(1), 37–52. <https://doi.org/10.1080/04353676.1991.11880331>
- Auel, C., Albayrak, I., Sumi, T., & Boes, R. M. (2017a). Sediment transport in high-speed flows over a fixed bed: 1. Particle dynamics. *Earth Surface Processes and Landforms*, 42(9), 1365–1383. <https://doi.org/10.1002/esp.4128>
- Auel, C., Albayrak, I., Sumi, T., & Boes, R. M. (2017b). Sediment transport in high-speed flows over a fixed bed: 2. Particle impacts and abrasion prediction. *Earth Surface Processes and Landforms*, 42(9), 1384–1396. <https://doi.org/10.1002/esp.4132>
- Bachelet, V., Mangeney, A., De Rosny, J., Toussaint, R., & Farin, M. (2018). Elastic wave generated by granular impact on rough and erodible surfaces. *Journal of Applied Physics*, 123(4), 044901.
- Badoux, A., Andres, N., & Turowski, J. (2014). Damage costs due to bedload transport processes in Switzerland. *Natural Hazards and Earth System Science*, 14(2), 279–294.
- Bakker, M., Costa, A., Silva, T. A., Stutenbecker, L., Girardclos, S., Loizeau, J. L., et al. (2018). Combined flow abstraction and climate change impacts on an aggrading Alpine river. *Water Resources Research*, 54, 223–242. <https://doi.org/10.1002/2017WR021775>
- Barrière, J., Krein, A., Oth, A., & Schenkluhn, R. (2015). An advanced signal processing technique for deriving grain size information of bedload transport from impact plate vibration measurements. *Earth Surface Processes and Landforms*, 40(7), 913–924. <https://doi.org/10.1002/esp.3693>
- Barrière, J., Oth, A., Hostache, R., & Krein, A. (2015). Bed load transport monitoring using seismic observations in a low-gradient rural gravel bed stream. *Geophysical Research Letters*, 42, 2294–2301. <https://doi.org/10.1002/2015gl063630>
- Boore, D. M., & Joyner, W. B. (1997). Site amplifications for generic rock sites. *Bulletin of the Seismological Society of America*, 87(2), 327–341.
- Buffington, J. M., & Montgomery, D. R. (1997). A systematic analysis of eight decades of incipient motion studies, with special reference to gravel-bedded rivers. *Water Resources Research*, 33(8), 1993–2029. <https://doi.org/10.1029/96wr03190>
- Burtin, A., Bollinger, L., Vergne, J., Cattin, R., & Nábělek, J. L. (2008). Spectral analysis of seismic noise induced by rivers: A new tool to monitor spatiotemporal changes in stream hydrodynamics. *Journal of Geophysical Research*, 113, B05301. <https://doi.org/10.1029/2007JB005034>
- Burtin, A., Cattin, R., Bollinger, L., Vergne, J., Steer, P., Robert, A., et al. (2011). Towards the hydrologic and bed load monitoring from high-frequency seismic noise in a braided river: The “torrent de St Pierre”, French Alps. *Journal of Hydrology*, 408(1), 43–53. <https://doi.org/10.1016/j.jhydrol.2011.07.014>
- Burtin, A., Hovius, N., & Turowski, J. M. (2016). Seismic monitoring of torrential and fluvial processes. *Earth Surf. Dynamics*, 4(2), 285–307. <https://doi.org/10.5194/esurf-4-285-2016>
- Chao, W.-A., Wu, Y.-M., Zhao, L., Tsai, V. C., & Chen, C.-H. (2015). Seismologically determined bedload flux during the typhoon season. *Scientific Reports*, 5, 8261. <https://doi.org/10.1038/srep08261>
- Chatanantavet, P., Whipple, K. X., Adams, M. A., & Lamb, M. P. (2013). Experimental study on coarse grain saltation dynamics in bedrock channels. *Journal of Geophysical Research: Earth Surface*, 118, 1161–1176. <https://doi.org/10.1002/jgrf.20053>
- Church, M. (2006). Bed material transport and the morphology of alluvial river channels. *Annual Review of Earth and Planetary Sciences*, 34, 325–354.
- Cook, K. L., Andermann, C., Gimbert, F., Adhikari, B. R., & Hovius, N. (2018). Glacial lake outburst floods as drivers of fluvial erosion in the Himalaya. *Science*, 362(6410), 53–57. <https://doi.org/10.1126/science.aat4981>

- Dietze, M., Lagarde, S., Halfi, E., Laronne, J. B., & Turowski, J. M. (2019). Joint sensing of bedload flux and water depth by seismic data inversion. *Water Resources Research*, 55, 9892–9904. <https://doi.org/10.1029/2019wr026072>
- Erickson, D., McNamara, D. E., & Benz, H. M. (2004). Frequency-dependent Lg Q within the continental United States. *Bulletin of the Seismological Society of America*, 94(5), 1630–1643. <https://doi.org/10.1785/012003218>
- Gimbert, F., Fuller, B. M., Lamb, M. P., Tsai, V. C., & Johnson, J. P. L. (2019). Particle transport mechanics and induced seismic noise in steep flume experiments with accelerometer-embedded tracers. *Earth Surface Processes and Landforms*, 44(1), 219–241. <https://doi.org/10.1002/esp.4495>
- Gimbert, F., Tsai, V. C., Amundson, J. M., Bartholomaus, T. C., & Walter, J. I. (2016). Subseasonal changes observed in subglacial channel pressure, size, and sediment transport. *Geophysical Research Letters*, 43, 3786–3794. <https://doi.org/10.1002/2016GL068337>
- Gimbert, F., Tsai, V. C., & Lamb, M. P. (2014). A physical model for seismic noise generation by turbulent flow in rivers. *Journal of Geophysical Research: Earth Surface*, 119, 2209–2238. <https://doi.org/10.1002/2014JF003201>
- Gomez, B., Naff, R. L., & Hubbell, D. W. (1989). Temporal variations in bedload transport rates associated with the migration of bedforms. *Earth Surface Processes and Landforms*, 14(2), 135–156. <https://doi.org/10.1002/esp.3290140205>
- Govi, M., Maraga, F., & Moia, F. (1993). Seismic detectors for continuous bed load monitoring in a gravel stream. *Hydrological Sciences Journal*, 38(2), 123–132. <https://doi.org/10.1080/02626669309492650>
- Habersack, H., Kreisler, A., Rindler, R., Aigner, J., Seitz, H., Liedermann, M., & Laronne, J. B. (2017). Integrated automatic and continuous bedload monitoring in gravel bed rivers. *Geomorphology*, 291, 80–93. <https://doi.org/10.1016/j.geomorph.2016.10.020>
- Hoey, T. (1992). Temporal variations in bedload transport rates and sediment storage in gravel-bed rivers. *Progress in Physical Geography: Earth and Environment*, 16(3), 319–338. <https://doi.org/10.1177/030913339201600303>
- Hsu, L., Finnegan, N. J., & Brodsky, E. E. (2011). A seismic signature of river bedload transport during storm events. *Geophysical Research Letters*, 38, L13407. <https://doi.org/10.1029/2011GL047759>
- Huang, C.-J., Yin, H.-Y., Chen, C.-Y., Yeh, C.-H., & Wang, C.-L. (2007). Ground vibrations produced by rock motions and debris flows. *Journal of Geophysical Research*, 112, F02014. <https://doi.org/10.1029/2005JF000437>
- Johnson, K. L. (1987). *Contact mechanics*. Cambridge, UK: Cambridge University Press.
- Kean, J. W., Coe, J. A., Coviello, V., Smith, J. B., McCoy, S. W., & Arattano, M. (2015). Estimating rates of debris flow entrainment from ground vibrations. *Geophysical Research Letters*, 42, 6365–6372. <https://doi.org/10.1002/2015GL064811>
- Kellerhals, R., & Bray, D. I. (1971). Sampling procedures for coarse fluvial sediments. *Journal of the Hydraulics Division*, 97(8), 1165–1180.
- Lai, V. H., Tsai, V. C., Lamb, M. P., Ulizio, T. P., & Beer, A. R. (2018). The seismic signature of debris flows: Flow mechanics and early warning at Montecito, California. *Geophysical Research Letters*, 45, 5528–5535. <https://doi.org/10.1029/2018gl077683>
- Lajeunesse, E., Malverti, L., & Charru, F. (2010). Bed load transport in turbulent flow at the grain scale: Experiments and modeling. *Journal of Geophysical Research*, 115, F04001. <https://doi.org/10.1029/2009JF001628>
- Lamb, M. P., Dietrich, W. E., & Sklar, L. S. (2008). A model for fluvial bedrock incision by impacting suspended and bed load sediment. *Journal of Geophysical Research*, 113, F03025. <https://doi.org/10.1029/2007JF000915>
- Lamb, M. P., Dietrich, W. E., & Venditti, J. G. (2008). Is the critical Shields stress for incipient sediment motion dependent on channel-bed slope? *Journal of Geophysical Research*, 113, F02008. <https://doi.org/10.1029/2007JF000831>
- Lane, S. N., Richards, K. S., & Chandler, J. H. (1996). Discharge and sediment supply controls on erosion and deposition in a dynamic alluvial channel. *Geomorphology*, 15(1), 1–15. [https://doi.org/10.1016/0169-555X\(95\)00113-J](https://doi.org/10.1016/0169-555X(95)00113-J)
- Mao, L., Carrillo, R., Escarriaza, C., & Iroume, A. (2016). Flume and field-based calibration of surrogate sensors for monitoring bedload transport. *Geomorphology*, 253, 10–21. <https://doi.org/10.1016/j.geomorph.2015.10.002>
- McNamara, D. E., & Buland, R. P. (2004). Ambient noise levels in the continental United States. *Bulletin of the Seismological Society of America*, 94(4), 1517–1527. <https://doi.org/10.1785/012003001>
- Misset, C., Recking, A., Legout, C., Bakker, M., Bodereau, N., Borgniet, L., et al. (2020). Combining multi-physical measurements to quantify bedload transport and morphodynamics interactions in an Alpine braiding river reach. *Geomorphology*, 351, 106877. <https://doi.org/10.1016/j.geomorph.2019.106877>
- Misset, C., Recking, A., Legout, C., Valsangkar, N., Bodereau, N., Zanker, S., et al. (2019). The dynamics of suspended sediment in a typical Alpine alluvial river reach: Insight from a seasonal survey. *Water Resources Research*, 55, 10,918–10,934. <https://doi.org/10.1029/2019wr025222>
- Mizuyama, T., Laronne, J. B., Nonaka, M., Sawada, T., Satofuka, Y., Matsuoka, M., et al. (2010). Calibration of a passive acoustic bedload monitoring system in Japanese mountain rivers. *US Geological Survey Scientific Investigations Report*, 5091, 296–318.
- Morozov, I. B. (2010). On the causes of frequency-dependent apparent seismological Q. *Pure and Applied Geophysics*, 167(10), 1131–1146. <https://doi.org/10.1007/s00024-010-0100-6>
- Park, C. B., Miller, R. D., Xia, J., & Ivanov, J. (2007). Multichannel analysis of surface waves (MASW)—Active and passive methods. *The Leading Edge*, 26(1), 60–64. <https://doi.org/10.1190/1.2431832>
- Parker, G. (1990). Surface-based bedload transport relation for gravel rivers. *Journal of Hydraulic Research*, 28(4), 417–436. <https://doi.org/10.1080/00221689009499058>
- Parker, G., & Klingeman, P. C. (1982). On why gravel bed streams are paved. *Water Resources Research*, 18(5), 1409–1423. <https://doi.org/10.1029/WR018i005p01409>
- Recking, A. (2009). Theoretical development on the effects of changing flow hydraulics on incipient bed load motion. *Water Resources Research*, 45. <https://doi.org/10.1029/2008WR006826>
- Rickenmann, D., Turowski, J. M., Fritschi, B., Wyss, C., Laronne, J., Barzilai, R., et al. (2014). Bedload transport measurements with impact plate geophones: Comparison of sensor calibration in different gravel-bed streams. *Earth Surface Processes and Landforms*, 39(7), 928–942. <https://doi.org/10.1002/esp.3499>
- Ritzwoller, M. H., & Levshin, A. L. (1998). Eurasian surface wave tomography: Group velocities. *Journal of Geophysical Research*, 103(B3), 4839–4878. <https://doi.org/10.1029/97jb02622>
- Rix, G. J., Hebel, G. L., & Orozco, M. C. (2002). Near-surface vs profiling in the New Madrid seismic zone using surface-wave methods. *Seismological Research Letters*, 73(3), 380–392. <https://doi.org/10.1785/gssrl.73.3.380>
- Roten, D., Cornou, C., Steimen, S., Fäh, D., & Giardini, D. (2004). 2D resonances in Alpine valleys identified from ambient vibration wavefield. Paper presented at the Proc. 13th World Conf. on Earthq. Engng., Vancouver, Canada BC.
- Roth, D. L., Brodsky, E. E., Finnegan, N. J., Rickenmann, D., Turowski, J. M., & Badoux, A. (2016). Bed load sediment transport inferred from seismic signals near a river. *Journal of Geophysical Research: Earth Surface*, 121, 725–747. <https://doi.org/10.1002/2015JF003782>

- Roth, D. L., Finnegan, N. J., Brodsky, E. E., Cook, K. L., Stark, C. P., & Wang, H. W. (2014). Migration of a coarse fluvial sediment pulse detected by hysteresis in bedload generated seismic waves. *Earth and Planetary Science Letters*, *404*, 144–153. <https://doi.org/10.1016/j.epsl.2014.07.019>
- Roth, D. L., Finnegan, N. J., Brodsky, E. E., Rickenmann, D., Turowski, J. M., Badoux, A., & Gimbert, F. (2017). Bed load transport and boundary roughness changes as competing causes of hysteresis in the relationship between river discharge and seismic amplitude recorded near a steep mountain stream. *Journal of Geophysical Research: Earth Surface*, *122*, 1182–1200. <https://doi.org/10.1002/2016JF004062>
- Schmandt, B., Aster, R. C., Scherler, D., Tsai, V. C., & Karlstrom, K. (2013). Multiple fluvial processes detected by riverside seismic and infrasound monitoring of a controlled flood in the Grand Canyon. *Geophysical Research Letters*, *40*, 4858–4863. <https://doi.org/10.1002/grl.50953>
- Schmandt, B., Gaeuman, D., Stewart, R., Hansen, S. M., Tsai, V. C., & Smith, J. (2017). Seismic array constraints on reach-scale bedload transport. *Geology*, *45*(4), 299–302. <https://doi.org/10.1130/G38639.1>
- Sklar, L. S., & Dietrich, W. E. (2004). A mechanistic model for river incision into bedrock by saltating bed load. *Water Resources Research*, *40*. <https://doi.org/10.1029/2003WR002496>
- Tsai, V. C., & Atiganyanun, S. (2014). Green's functions for surface waves in a generic velocity structure. *Bulletin of the Seismological Society of America*, *104*(5), 2573–2578. <https://doi.org/10.1785/0120140121>
- Tsai, V. C., Minchew, B., Lamb, M. P., & Ampuero, J.-P. (2012). A physical model for seismic noise generation from sediment transport in rivers. *Geophysical Research Letters*, *39*, L02404. <https://doi.org/10.1029/2011GL050255>
- Turowski, J. M., & Bloem, J.-P. (2016). The influence of sediment thickness on energy delivery to the bed by bedload impacts. *Geodinamica Acta*, *28*(3), 199–208. <https://doi.org/10.1080/09853111.2015.1047195>
- Vericat, D., Church, M., & Batalla, R. J. (2006). Bed load bias: Comparison of measurements obtained using two (76 and 152 mm) Helley-Smith samplers in a gravel bed river. *Water Resources Research*, *42*, W01402. <https://doi.org/10.1029/2005wr004025>
- Welch, P. (1967). The use of fast Fourier transform for the estimation of power spectra: A method based on time averaging over short, modified periodograms. *IEEE Transactions on Audio and Electroacoustics*, *15*(2), 70–73.
- Williams, R. D., Rennie, C. D., Brasington, J., Hicks, D. M., & Vericat, D. (2015). Linking the spatial distribution of bed load transport to morphological change during high-flow events in a shallow braided river. *Journal of Geophysical Research: Earth Surface*, *120*, 604–622. <https://doi.org/10.1002/2014jf003346>
- Wyss, C. R., Rickenmann, D., Fritschi, B., Turowski, J. M., Weitbrecht, V., & Boes, R. M. (2016). Laboratory flume experiments with the Swiss plate geophone bed load monitoring system: 1. Impulse counts and particle size identification. *Water Resources Research*, *52*, 7744–7759. <https://doi.org/10.1002/2015wr018555>